Evaluation of the interface of metallic-coated biodegradable polymeric stents with prokaryotic and eukaryotic cells

Ana M. Sousa [a], Rita Branco [b], Paula V. Morais [b], Manuel F. Pereira [c], Ana M. Amaro [a], Ana P. Piedade [a,*]

[a] University of Coimbra, CEMMPRE, Department of Mechanical Engineering, 3030-788, Coimbra, Portugal
[b] University of Coimbra, CEMMPRE, Department of Life Sciences, 3000-456, Coimbra, Portugal
[c] University of Lisbon, CERENA, Instituto Superior Técnico, Av. Rovisco Pais, 1, 1049-001, Lisboa, Portugal

ARTICLE INFO

ABSTRACT

Polymeric coronary stents, like the ABSORB™, are commonly used to treat atherosclerosis due to their bioresorbable and cell-compatible polymer structure. However, they face challenges such as high strut thickness, high elastic recoil, and lack of radiopacity. This study aims to address these limitations by modifying degradable stents produced by additive manufacturing with poly(lactic acid) (PLA) and poly(ε-caprolactone) (PCL) with degradable metallic coatings, specifically zinc (Zn) and magnesium (Mg), deposited via radiofrequency (rf) magnetron sputtering. The characterisation included the evaluation of the degradation of the coatings, antibacterial, anti-thrombogenicity, radiopacity, and mechanical properties.

The results showed that the metallic coatings inhibited bacterial growth, though Mg exhibited a high degradation rate. Thrombogenicity studies showed that Zn-coated stents had anticoagulant properties, while Mg-coated and controls were thrombogenic. Zn coatings significantly improved radiopacity, enhancing contrast by 43 %. Mechanical testing revealed that metallic coatings reduced yield strength and, thus, diminished elastic recoil after stent expansion. Zn-coated stents improved cyclic compression resistance by 270 % for PCL stents, with PLA-based stents showing smaller improvements. The coatings also enhanced crush resistance, particularly for Zn-coated PCL stents.

Overall, Zn-coated polymers have emerged as the premier prototype due to their superior biological and mechanical performance, appropriate degradation during the stent life, and ability to provide the appropriate radiopacity to medical devices.

1. Introduction

To reduce mortality resulting from atherosclerosis, percutaneous coronary intervention (PCI) combined with coronary stents has become a cornerstone of cardiovascular treatment. Drug-eluting stents (DES) are widely regarded as the standard in the cardiovascular field. These stents typically feature a permanent metallic structure, often made of cobalt-chromium alloy (CoCr), and a degradable polymeric coating that releases pharmaceutical drugs to prevent adverse biological responses following stent placement [1]. However, the permanent metallic structure can still elicit biological reactions once the polymeric coating degrades, potentially leading to artery re-blockage due to in-stent biological events and subsequent heart failure [2,3]. In response to these challenges, polymeric bioresorbable stents (BRS) have been developed.

They offer improved cellular compatibility and fewer adverse biological reactions than their metallic counterparts. Nevertheless, achieving mechanical properties comparable to DES requires thicker stents, which, in turn, can provoke adverse host responses [2,3]. Recent developments in stent design aim to tackle challenges by reducing the thickness of bioresorbable stents without compromising their mechanical integrity. Research indicates that adjusting design parameters can enhance mechanical support while minimising thickness and elastic recoil ratio [2,4,5].

Another significant limitation of polymeric BRS is the lack of radiopacity [6,7]. Coronary stents must exhibit adequate radiopacity to ensure device visibility through imaging techniques during surgical procedures for precise stent deployment and positioning into the artery [5,8]. To address this problem, several authors propose incorporating

---

radiopaque markers or coatings made from materials such as gold (Au), tantalum (Ta), or platinum (Pt) into the base structure of the stent [6,7,9]. Regardless, the markers may leach from the device during degradation and, since they are non-degradable, might lead to blockages in arteries or deposition in other organs, increasing the risk of fatality [6]. Therefore, developing alternative solutions that improve both safety and efficacy is compulsory. Emphasizing the bulk and surface properties is crucial to achieving optimal performance in coronary stents [10,11].

A promising approach that can solve some of the mentioned limitations involves polymeric BRS surface modification that simultaneously mitigates adverse biological responses [10,12]. This modification can be achieved through physical routes, like introducing surface micro- and nano-features, or chemical changes, such as coating with organic or inorganic materials [13].

Inorganic coatings, including metallic materials, are being explored as potential solutions to enhance the performance of medical devices in biological environments [14]. Research suggests that metallic coatings can significantly improve hydrophilicity, endothelial cell adhesion, proliferation, and antibacterial and anti-thrombogenic properties [14,15]. Various ceramic coatings, such as iridium oxide, titanium oxide, and carbon-based coatings, have been recommended to enhance cellular compatibility [16]. Additionally, metallic materials such as titanium (Ti) alloys, CoCr alloys, aluminium (Al) alloys, silver (Ag), or Au have shown potential as coatings for medical devices [12,16,17]. Conversely, these coatings were primarily used on permanent metallic stents, which do not degrade over time. Therefore, new materials are needed to coat bioresorbable stents. One possible solution is to use a metallic degradable coating such as iron (Fe), Mg, or Zn. These metallic materials and their alloys have emerged as promising bioresorbable materials, with numerous studies highlighting their suitable mechanical properties, cellular compatibility, and degradation profiles [1,18,19]. The degradation products of Mg or Zn play essential roles in various cellular activities, making them attractive candidates for improving the cellular compatibility and mechanical properties of bioresorbable stents [20–23]. For instance, Pan et al. [19] indicated in their study that Zn is a beneficial element that plays a crucial role in regulating the physiological microenvironment *in vivo*, boosting cellular compatibility. Additionally, Heakal and colleagues [24] referred to Mg as vital for metabolic processes as it is a co-factor in many enzymes and is a crucial component of the ribosomal machinery that translates genetic information into polypeptides. These characteristics make Zn and Mg materials potentially valuable for cardiovascular devices. Comparing Mg and Zn with Fe, the first two are more appropriate since research indicates that Fe and its alloys exhibit relatively slow degradation, producing insoluble degradation products that remain in physiological environments [25]. Furthermore, an excess of free iron in the bloodstream can lead to several pathological consequences for the organism, one of which is the formation of methemoglobin, a biomarker that can trigger oxidative processes in the blood [26]. Iron-mediated toxicity is primarily associated with Fe(II), which can react with oxygen to produce free radicals that damage macromolecules and result in cell death [27].

Sputtering technologies offer a powerful method for creating custom surfaces with optimised properties for specific applications, surpassing traditional chemistry boundaries [28,29]. The versatility and effectiveness of sputtering in producing high-quality coatings make it particularly advantageous for coronary stents. To date, and according to the literature survey, only a study by Xiao and colleagues [30] has explored using rf magnetron sputtering to deposit a nano-thick Au film onto a polymeric coronary stent. Although this coating improved the mechanical properties, the limited dissolution of gold in the human body poses risks such as arterial blockages and organ deposition, potentially leading to fatal outcomes [6]. Therefore, future research should focus on utilising the metallisation of polymers to enhance the performance of polymeric BRS and to explore alternative methods for creating fully degradable stents. Consequently, degradable metallic coatings, composed of Mg and Zn, present a promising path compared to the current non-degradable metallic coatings and radiomarkers, owing to their advantageous *in vivo* degradability, possible radiopacity and distinguishing them from conventional coatings [9,30,31].

This research aimed to show that the properties and characteristics of polymeric coronary stents, including the interface with biological fluid, can be improved by applying a coating of biodegradable metallic materials, specifically pure magnesium and zinc (Mg and Zn). Consequently, previously designed polymeric stents —PLA and PCL [2] – were produced through fused filament fabrication (FFF) additive manufacturing technology and then modified with a functional metallic coating (Mg and Zn). The study also delves into the biological characteristics, radiopacity, and mechanical performances of the coated stents. These coatings are anticipated to leverage the benefits of degradable polymeric and metallic materials, representing an innovative approach to cardiovascular intervention due to the possible creation of a fully degradable stent.

2. Experimental section

2.1. Materials

The PLA pellets (3D870) were purchased from Smartfill®, Spain, while the PCL filament was acquired from 3D4Makers®, the Netherlands, with an average diameter of 1.75 mm. The magnesium (99.999 %) and zinc (99.999 %) were purchased from Codex International with a diameter and thickness of 100 mm and 3 mm, respectively. The pure monocrystalline silicon waffles (100) were acquired in Siegert Waffer, Germany. The sputtering gas, Ar 99.9999 % purity, was acquired from Trinac, Portugal.

2.2. Additive manufacturing technology

FFF technology was used to print the coronary stents, and the design was developed according to previous studies [2]. The test specimens and stents were printed using Robo R2 equipment with a closed chamber [3]. All printing parameters were selected based on previously published works [2,3] to ensure that the printing parameters allow the best set of properties for coronary stents. The prototypes were printed according to
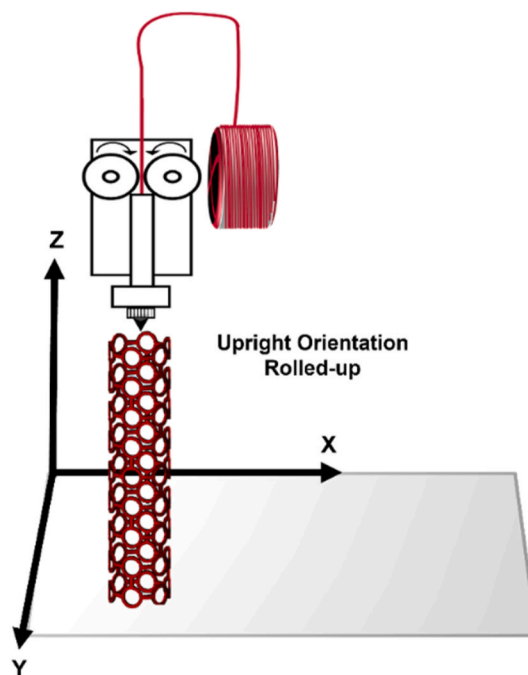

Fig. 1. Schematic representation of the building orientation of 3D-printed coronary stents (supports are not visible).

the schematic representation displayed in Fig. 1 with supports that were removed after the specimen was printed. The main printing parameters used for this work are displayed in Table 1.

2.3. Sputtering technology

The Mg and Zn coatings were deposited by rf magnetron sputtering in an Edwards 360 equipment. Two rf power supplies of 600 and 500 W were connected to the magnetron target and cooled substrate holder, respectively. The metallic targets (100 mm diameter, 3 mm thickness, and 99.99 % purity) were acquired from Goodfellow and used in a non-reactive Ar 99.9999 % purity atmosphere. Monocrystalline silicon (10 x 10 × 0.5 mm) and polymeric printed stents and samples were used as substrates. The silicon substrates were previously ultrasonically cleaned with ketone, alcohol, and Milli-Q water for 10 min in each liquid. The polymeric substrates were cleaned in isopropanol and Milli-Q water in an ultrasound bath for 10 min in each liquid. The ultimate base pressure of the vacuum chamber was $1x10^{-4}$ Pa. Before the deposition, the samples and the targets were cleaned for 5 min at 150 W, with a working pressure of 0.5 Pa, and a shutter was placed between them to avoid cross-contamination. The deposition parameters used to produce the Mg and Zn coatings are presented in Table 2.

2.4. In vitro evaluation

2.4.1. Immersion tests

The degradation profile was evaluated by immersion in a modified Simulated Blood Plasma (SBP) solution that mimics the inorganic content of human blood plasma (HBP) (Table 3) [32]. The tests were conducted at 37 °C and 100 rpm for 15 days in a Benchmark thermoshaker. At regular intervals, the solutions from the duplicates were renewed, and the samples and the liquid were analysed. Additionally, the results were compared with those obtained by replicating the entire experience but using Milli-Q water as immersion fluid to observe if the ionic inorganic composition and concentration influenced the degradation rate. The coatings were evaluated on a monocrystalline silicon substrate since it is a standard and common procedure to analyse the properties and characteristics of the coatings without the interference of several variable substrate characteristics (such as roughness) before depositing them onto polymers. The aim was to evaluate the degradation profile of the coating itself [33–35].

Scanning electron microscopy (SEM) observation coupled with energy dispersive spectroscopy (EDS) was performed to characterise the morphology of the surface of the films and to analyse the elemental composition after the degradation in SBP and Milli-Q. Chemical analysis of the surfaces was also performed using microRaman spectroscopy. The spectra were collected in a Renishaw in Via Reflex Microscope (UK) coupled to a Leica microscope (DM2700 M) at room temperature, in a 100-2000 cm^{-1} spectral range, with a 532 nm laser, and a spectral resolution was 2 cm^{-1} using an ×50 objective lens. The exposure time was 20 s, and the laser intensity was kept at 10 % of the maximum power (50 mW) to avoid surface degradation. The software from Renishaw's WiRE™ was used to acquire the spectra and analyse all samples.

Additionally, pH measurements were done at the indicated times of refreshing the solution. Aliquots of solution were collected at different times to quantify the concentration of Mg^{2+} and Zn^{2+} through Flame Atomic Absorption Spectroscopy (AAS) using an Analytik Jena – ContrAA 300 Instrument. It is worth noting that the modified SBP solution was made without Mg to facilitate the AAS analysis.

2.4.2. Antibacterials tests

The antibacterial tests were conducted using polymeric specimens printed with the dimensions recommended by previous studies as the ideal to understand the material response: 10 x 10 × 2 mm^3 [36,37]. Some of the printed specimens were coated with Mg and Zn, according to what was described in section 2.3. The coated and control polymeric materials underwent a 30-min sterilisation process using UV-C (254 nm) (Fig. 2A). Three clinically relevant reference strains, *Staphylococcus aureus* ATCC25923 *(S. aureus)*, *Pseudomonas aeruginosa DSM1117 (P. aeruginosa)* and *Escherichia coli* ATCC25922 *(E. coli)*, were assessed [38]. The bacterial strains were resuspended in phosphate-buffered saline (PBS) solution to achieve an optical density of approximately 0.2 (10^8 cells·mL^{-1}). A volume of 80 μL was then applied to the surfaces to evaluate cell survival upon surface contact (A = 100 mm^2) with the uncoated and coated polymers and incubated at 37 °C for 24 h. The specimens were then washed with sterile PBS (10 mL), and the adherent bacteria on the scaffolds were removed by ultrasonication for 3 min. The solution collected post-ultrasonication underwent a serial dilution process in PBS. From 10^{-1}, 10^{-2} and 10^{-3} bacterial dilutions, 0.1 mL of suspensions were plated on tryptone soy agar (TSA) medium and allowed to incubate at 37 °C for 24 h to determine the number of colony-forming units (CFU) (Fig. 2B). The antibacterial efficiency (AE %) was determined for the same dilution using Equation (1), with B and A denoting the total number of bacterial colonies in the uncoated samples (control) and coated samples, respectively [39] (see Fig. 3).

$$AE(\%) = \frac{B - A}{B} \times 100$$

Equation 1

2.4.3. Blood clotting assays

The *in vitro* blood clotting experiments were conducted based on previously reported methods with some adjustments [40,41]. The uncoated and coated polymers were first printed as cubes (10 x 10 × 2 mm^3) with a face area of 100 mm^2 and were coated with Mg and Zn, according to what was described in section 2.3. Then, the samples were arranged in multi-well plates. Subsequently, 100 μL of blood treated with sodium citrate (ACD) was carefully applied to the surface of each sample, followed by the addition of 10 μL of [CaCl$_2$] = 0.1 M to initiate the blood clotting process. The samples were then left to incubate at 37 °C for 60 min; after, 2 mL of Milli-Q water was gently added to the surfaces to halt the coagulation process while preserving the formed clots. At least three samples of each condition were tested. After 10 min of incubation at 37 °C, the haemoglobin (Hb) was released from haemolysed red blood cells, not integrated into the formed clots, and the absorbance of the solution was measured at 540 nm (Abs$_{sample}$) using a UV–vis spectrophotometer. The absorbance of 100 μL ACD-treated blood diluted in 2 mL of Milli-Q water served as a positive control (Abs$_{positivecontrol}$), while Milli-Q water was used as the negative control. Finally, the blood clotting index (BCI) of the samples was calculated according to Equation (2) [40].

$$BCI(\%) = \frac{Abs_{sample}}{Abs_{positive\ control}} \times 100$$

Equation 2

The blood clot formed was collected, and its mass was measured. The percentage of thrombogenicity (%) was calculated using Equation (3) [40].

$$Thrombogenicity\ (\%) = \frac{M_{sample} - M_{negative\ control}}{M_{positive\ control} - M_{negative\ control}} \times 100$$

Equation 3

Table 1
Printing parameters for the polymeric stents.

Material	$T_{printing}$ (°C)	T_{bed} (°C)	$V_{printing}$ (mm•s^{-1})	Layer Height (mm)	Shell	Infill Density (%)	Infill Pattern
PLA	200	60	60	0.1	1	100	Lines
PCL	130	30	10	0.1	1	100	Lines

Table 2

Optimised deposition parameters for the metallic coatings.

Material	Power density (W•mm^{-2})	Deposition pressure (Pa)	Deposition time (min)	Thickness of the Coating (µm)
Mg (99.999 %)	2 x 10^{-2}	0.7	30	0.7
Zn (99.999 %)		0.4	30	2.1

Table 3

Chemical composition of the simulated blood plasma (SBP) solution (Adapted from Ref. [32]).

Ion	Concentration (mM)	
	HBP	SBP
Na^+	142	143
K^+	5.0	5.0
Mg^+	1.5	–
Ca^{2+}	2.5	2.5
Cl^-	103	123
HCO_3^-	27	27
HPO_4^{2-}	1.0	1.0
SO_4^{2-}	0.5	0.5

Images of the clot in each surface and the surface after blood contact were captured using a 3D digital microscope, Hirox HR-5000, and the Hirox RX-100 software. The human whole blood used in the study was obtained from healthy volunteers who had not taken any medications. They provided full informed consent according to the declaration of Helsinki [42]. The blood was collected through venipuncture using sterilised S-Monovette® Citrate 9NC 0.106 mol L^{-1} 3.2 % tubes (SARSTEDT AG & Co. KG, Nümbrecht, Germany) containing buffered sodium citrate (0.106 M). The first tube of blood collected was discarded.

2.5. Radiopacity evaluation

Assessing the radiopacity of medical devices is a critical step in their development to ensure visibility during procedures. Radiopacity refers to the ability of the material to block radiation, making an object visible in medical images. This visibility is essential for tracking invasive devices during medical procedures and identifying any remaining parts. According to ASTM F640-20 ("Standard Test Methods for Determining Radiopacity for Medical Use"), the radiopacity of a medical device can be determined through various techniques, such as computed tomography (CT) scans. Radiopacity can be evaluated qualitatively by comparing images of a test specimen with a user-defined standard or quantitatively by determining the specific difference in optical density or pixel intensity between the test specimen and the standard [43].

This research used µ-CT to study the radiopacity of stents, with uncoated samples as the standard, given their proven radiolucency [8]. All samples were scanned using the µ-XCT Skyscan 1172 microtomograph (Bruker Instruments, Inc., Billerica, MA, USA) by rotating the sample over 180° with a variable rotation step of 0.20–0.30° depending on the selected resolution, according to the sample size. The acquisition conditions were optimised to achieve the best image contrast. The acquired data was then processed and analysed using NRecon®1.6.3 routine, volumetric visualisation was achieved with DataView® and CTvox® programs by Bruker, and the pixel intensity was determined using Image J. This acquisition and processing method was previously developed by Pereira et al. [44–46] and Table 4 lists some of the parameters used during the scanning procedure.

2.6. Mechanical characterisation

2.6.1. Tensile test

The stents for tensile tests were produced according to the specifications of a previous study [2]. Fig. 4 depicts a scheme of the printed
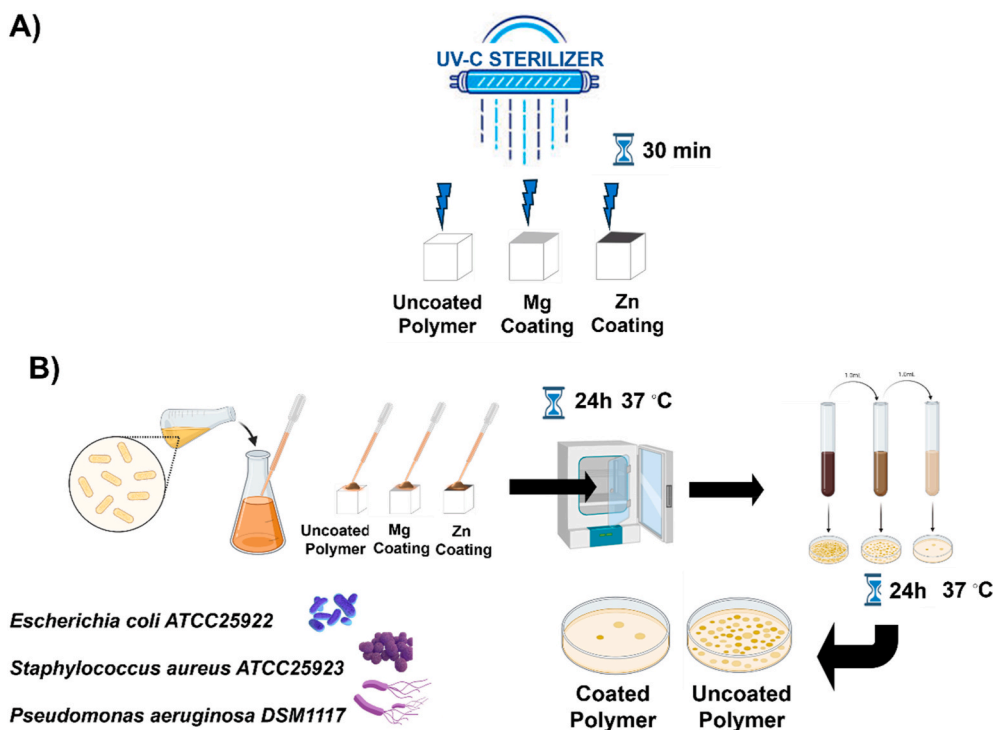
Fig. 2. Schematic representation of the quantitative analysis of antibacterial activity: A) UV-C sterilisation; B) representation of the steps of serial dilution and plating to analyse cell number by colony forming unit (CFU).
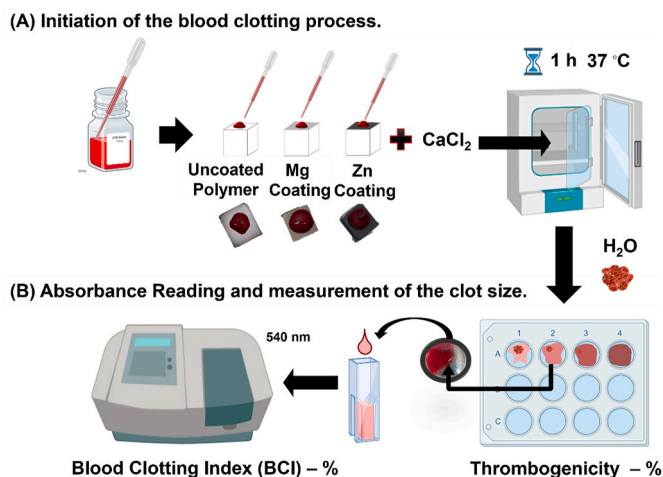
Fig. 3. Schematic representation of the blood clotting assays.

Table 4
Summary of the parameters used in the scanning procedure.

Parameters	
Pixel size	2.5–3.8 μm
Filament Current	113–131 μA
Voltage	70–85 kV
Power	10 W
Exposure time	1900–2100 ms
Number of Images	737–1105
File Type	16-bit
Scan Duration	2h30-3h00

specimens used for the tensile tests. The scheme shows a scale seven times larger than the original design (Fig. 4A), and the macrographs in Fig. 4B illustrate how the specimens were positioned in the equipment.

The tensile tests were performed utilising an INSTRON® 68TM-5 universal tensile testing machine with a 5 kN load cell. The tests were executed at a rate of 0.025 mm·min^{-1} under ambient conditions. Integrating a dual measurement multimeter model GDM-8351 from GwInstek in 4 W configuration into the tensile machine allowed for the measurement of the electrical resistance of the samples during the tensile testing (Fig. 5). A minimum of three samples of each polymeric material, uncoated and coated with Mg and Zn, were tested. The acquired data was filtered in Matlab_R2022b using a second-order Savitzky-Golay filter. Subsequently, the acquired results were analysed using the OriginPro® 2018 software. Fig. 5 illustrates a schematic diagram for measuring the electrical resistance of the coated polymers.
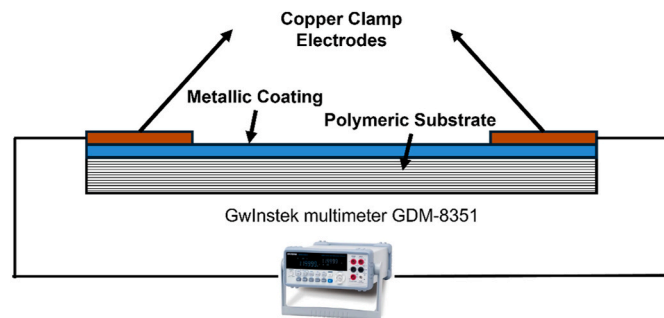

Fig. 5. Cross-section schematic diagram for measuring the electrical resistance of the coated polymers.

2.6.2. Compressive test

The stents used for the cyclic compressive test were produced with the specifications of a previous study [2]. The devices, four times larger than the original design, both coated and uncoated, were arranged horizontally on the testing platform and subjected to repeated compression and expansion cycles to mimic arterial vasomotion. Each cycle consisted of compressing the stent to 25 % of its original diameter and then allowing its expansion back to its original size, repeated five times. After each cycle, the stent was held in the compressed or expanded state for 10 s to ensure complete compression and expansion. The changes in the hysteresis loop area and the elasticity after five cycles were compared transversely to all samples, and the results were evaluated according to previous studies [31].

Subsequently, in another experimental characterisation, the stent was further compressed until it reached 50 % of its diameter, at which point the stent was crushed, as described in various studies and according to the standard ISO 25539-2 ("Cardiovascular implants — Endovascular devices – Part 2: Vascular Stents") [31,47,48]. During the compression test, the compressive force was applied in the radial direction of the stent, which was perpendicular to its axis. The compressive force was normalised by dividing the force by the stent length to simplify comparisons between coated and uncoated stents. The normalised force of the stent material (per unit length) F_{CN} (N·mm^{-1}) was calculated as a function of displacement (mm). Fig. 6 displays a schematic representation to illustrate how the specimens were positioned in the equipment and how the tests were performed (cyclic compression and crush resistance).

The cyclic test and crush resistance were performed utilising a Shimadzu Autograph AGS-X, outfitted with a 5 kN load cell. The tests were executed at a strain rate of 0.5 mm·min^{-1} under ambient conditions. At least five specimens of each condition were tested.
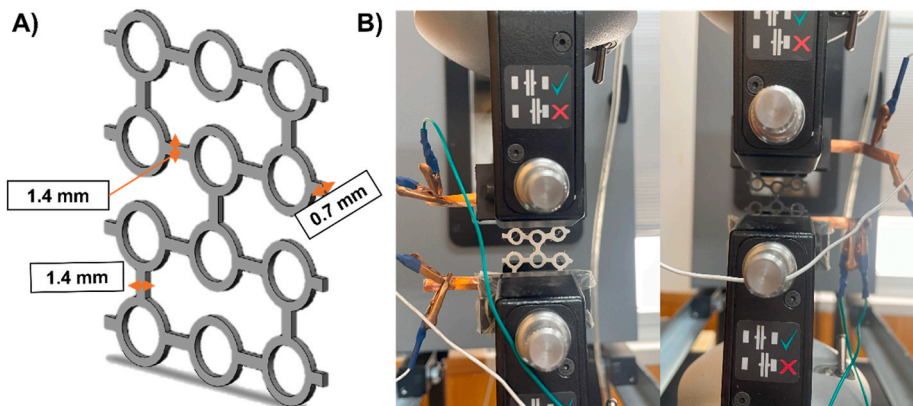

Fig. 4. Schematic representation of the tensile specimens (a) and macrographs of the equipment (b).
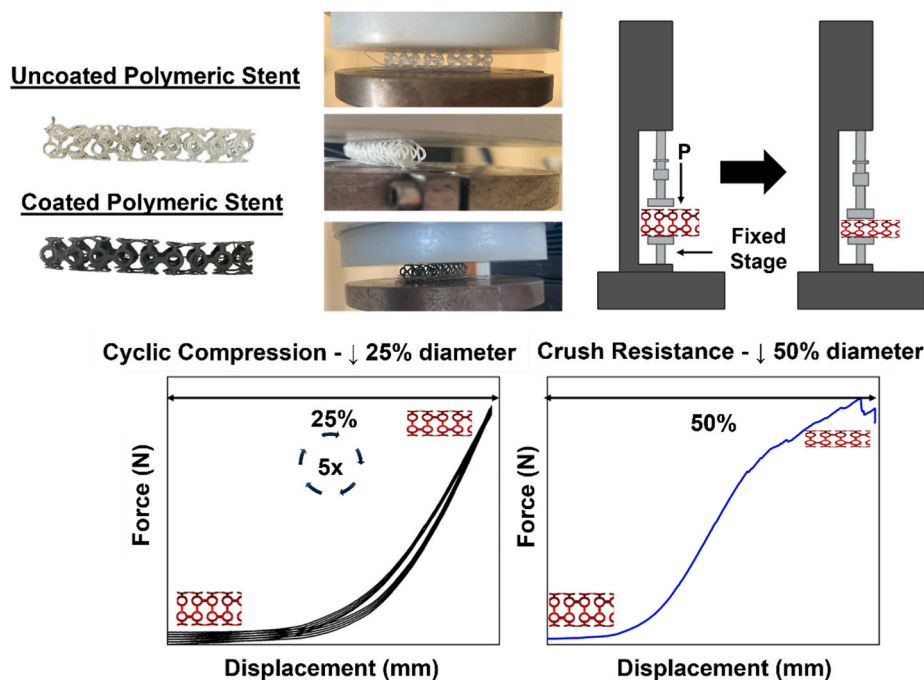
Fig. 6. Schematic representation of cyclic compression test and crush resistance test.

2.7. Statistical analysis

Statistical analyses were performed for the assays, and the results were presented as mean ± standard deviations. Statistical differences were analysed using a one-way Analysis of Variance (ANOVA) with a Turkey post-hoc test, performed using GraphPad Prism® version 5 software (GraphPad Software Inc., La Jolla, CA, USA). Differences were considered statistically significant at $p < 0.05$. The statistical significance was indicated using the symbol (*). Significance results are also indicated according to p values with one, two, three, or four of the symbols (*) corresponding to $0.01 < p < 0.05$, $0.001 < p < 0.01$, $0.0001 < p < 0.001$ e $p < 0.0001$.

3. Results and discussion

3.1. Characterisation post-degradation

Biodegradable stents and their coatings are surrounded by blood and tissue fluid, which contains various inorganic species, for instance, Cl-, HPO42- or HCO3-. As the coatings are intended to degrade over time, it is crucial to assess the rate of degradation influenced by these compounds and to identify the main corrosion products resulting from the ionic exchanges occurring on the surface of the coatings, as already done in several published articles [24,49–51]. The study examined the behaviour of the two metallic coatings (Mg and Zn) in an aqueous media. Milli-Q water was utilised as a control, and SBP was used to replicate the inorganic components of blood and their effects on coating degradation.

SEM/EDS (Fig. 7, Figs. 8 and 9), Raman spectroscopy (Fig. 10), pH measurements (Fig. 11), and AAS (Fig. 12) were carried out on the surfaces and media at various time intervals to analyse the degradation behaviour of the different surfaces. The EDS analysis lacks standardisation, but the study was conducted on multiple samples under the same observation parameters, allowing for comparison of results to identify trends and evaluate relative semi-quantitative chemical composition besides qualitative spectra for identifying elements [52].
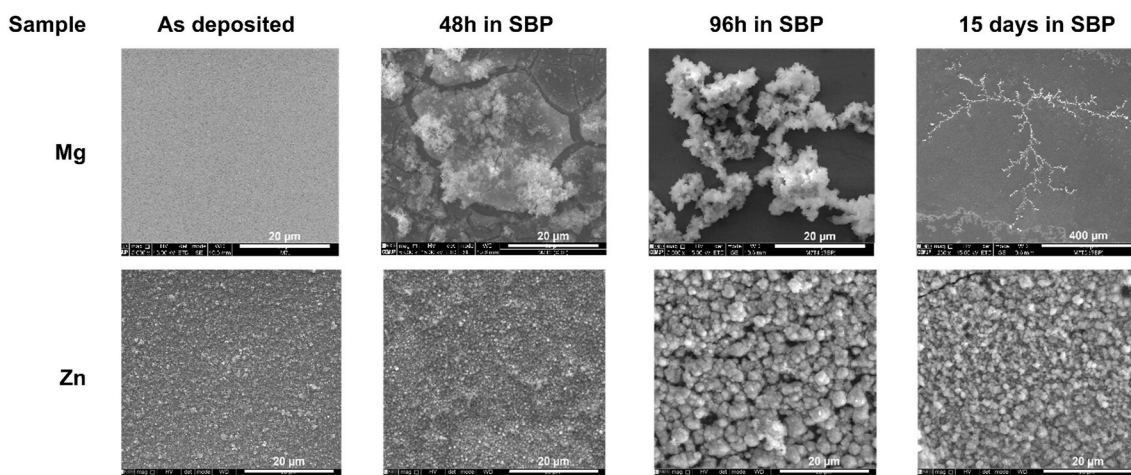

Fig. 7. Surface micrographs of Mg and Zn coatings through the degradation process in SBP (Secondary electrons – SE).
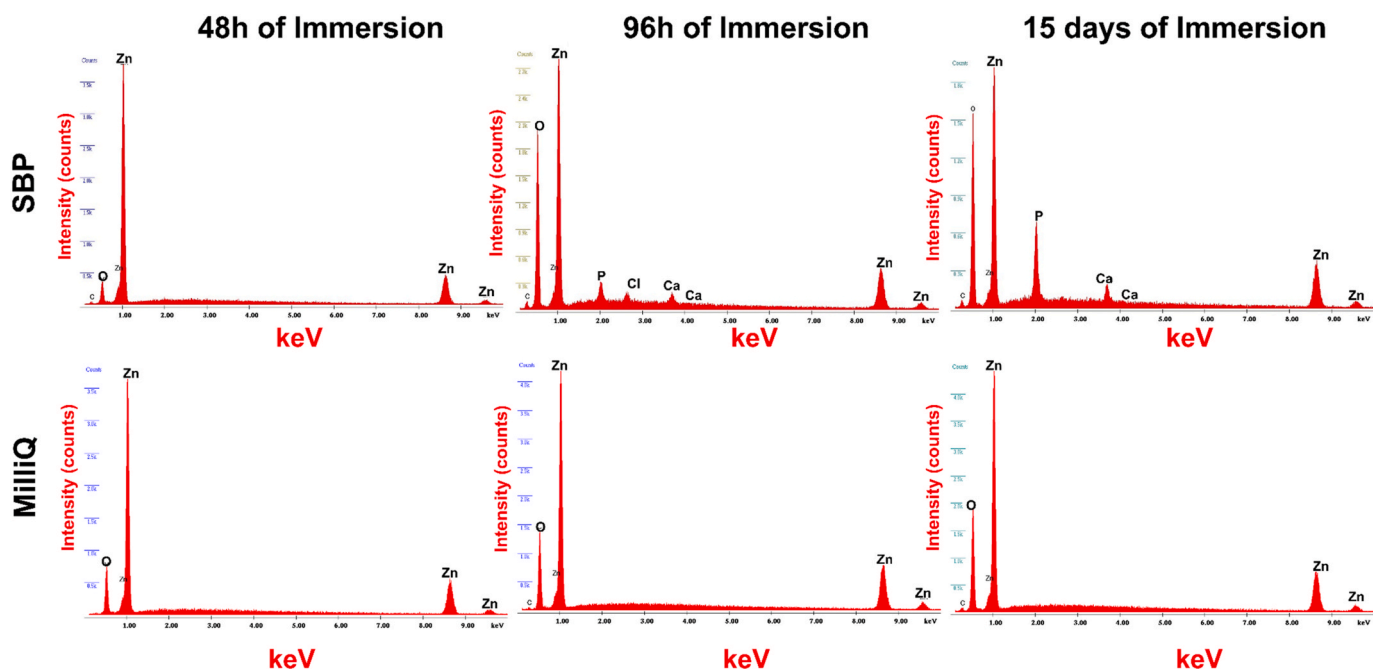
Fig. 8. EDS spectra for Zn surfaces after 48h, 96h and 15 days immersion in SBP and Milli-Q.
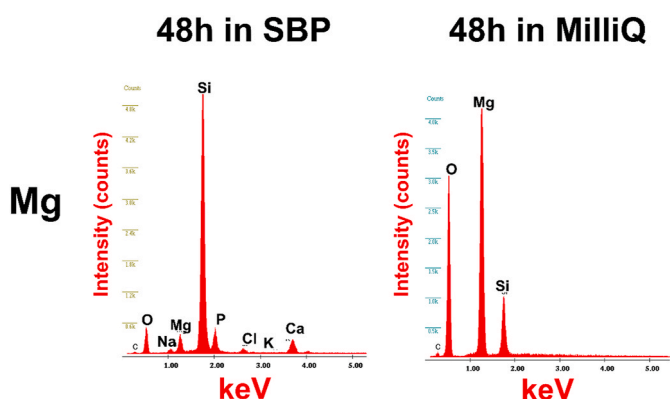

Fig. 9. EDS spectra for Mg coatings after an immersion of 48h in Milli-Q and SBP.

In this study, only the degradation profile of the metallic films was examined because PLA and PCL are commonly used as biodegradable polymers in coronary stents, with well-established and studied degradation times ranging from 18 to 30 months for PLA and 24–36 months for PCL [3,53].

3.1.1. Mg coatings

Magnesium is widely used in the medical field because it is essential for metabolic processes in the human body. In the present study, we investigated the potential use of magnesium coatings to enhance the properties of coronary stents. We found that the Mg surfaces immersed in SBP exhibited a significantly higher degradation rate than those tested in Milli-Q (Fig. 9 and Figure S1 – Supplementary Information). This indicates that the inorganic components in SBP have a notable impact on the morphology of films, promoting film degradation. The EDS analysis revealed that the atomic percentage (at.%) of magnesium was much lower on the surfaces tested in SBP compared to those in Milli-Q water. SEM/EDS results also confirmed that the films were nearly degraded after 48 h in SBP.

Moreover, the Raman spectra of the surface of the coatings submerged in SBP reveal that the quantity of ionic magnesium must be too low as the signal of magnesium-containing molecules is undetected. On the other hand, a high peak related to the silicon substrate (521 cm^{-1}) was detected, revealing that almost all of the film was degraded after 48 h of immersion [54]. Regarding the remaining film on the substrate, the peak at around 970 cm^{-1} is related to the Ca−P derivates. Another weak
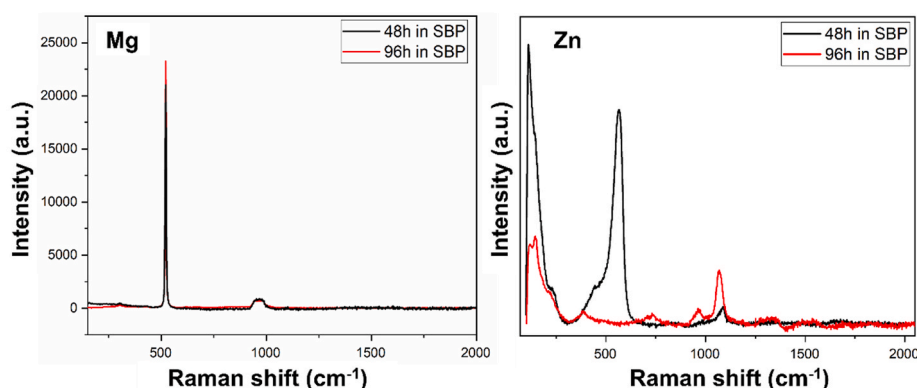

Fig. 10. Raman spectra of Mg and Zn coatings after the immersion test in SBP for 96h at 37 °C.
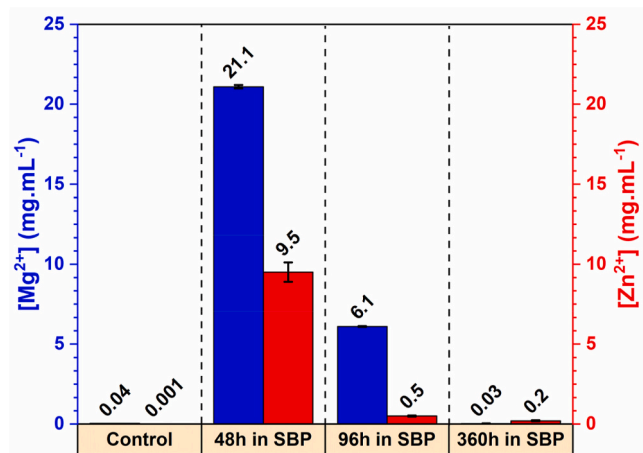
Fig. 11. Mg^{2+} and Zn^{2+} concentration in the immersion fluid during the degradation of the coatings in SBP at 37 °C.
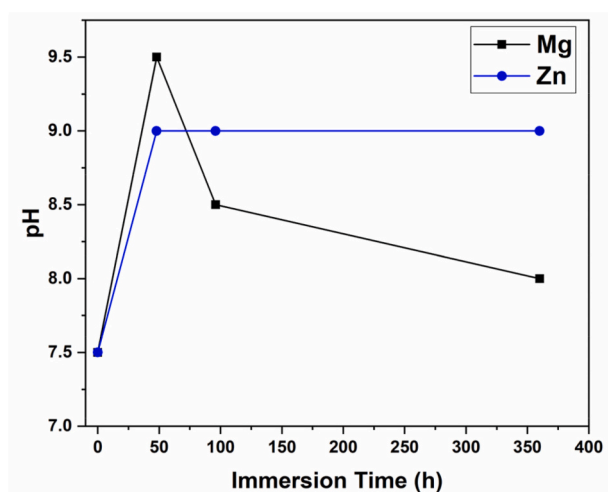

Fig. 12. pH values of the SBP solution during the degradation of the magnesium and zinc coatings at 37 °C (15 days–360h).

peak (~300 cm^{-1}) appears after 48 h, corresponding to the CaO stretching vibration [55,56]. When analysing the films that were submerged in Milli−Q water (Figure S2 – Supplementary Information), the Raman spectra show the typical peaks of the presence of magnesium oxide (MgO) and brucite ($Mg(OH)_2$) as predicted by the Pourbaix diagram [57]. Additionally, it shows the surface phonon vibrations of magnesium, its oxides, and hydroxides [55,58].

The investigation of the degradation deposits reveals that, after 48 h of immersion in SBP, the Mg surfaces displayed a mixture of sandy, sharp, flat, and cracked surfaces as precipitates (Fig. 7). Shafyra and colleagues [59] noted in their study the presence of quite similar precipitates resulting from the degradation of Mg-based materials. They found that the sandy structures were likely to correspond to Ca−P−derived compounds, while the flat and cracked surfaces were linked to the presence of $Mg(OH)_2$. Despite the lack of Raman spectra peaks to support the presence of $Mg(OH)_2$ (perhaps due to their low concentration) the SEM/EDS analysis confirmed the presence of Mg and O chemical elements, which might be related to the formation of brucite (Fig. 9) [59]. However, the exact quantification of $Mg(OH)_2$ due to the degradation process must be confirmed using other characterization techniques such as X-ray Photon Spectroscopy (XPS). Nonetheless, it was not a priority to precisely identify the precipitates as the existing literature clearly states that the degradation products of Mg are

cytocompatible, as previously mentioned. Furthermore, it inferred that the dehydration of the precipitates during the sample preparation process, which involved a drying stage, led to the formation of cracks [59]. The presence of Ca−P compounds was also confirmed by the EDS semi-quantitative analysis through the identification of Ca (4 at.%) and P (6 at.%) (Fig. 9), indicating a rich-phosphate layer, as the atomic percentage of phosphate is higher than that of calcium [60]. After 96 h, only a small amount of magnesium and SBP derivatives remained on the surface.

As previously mentioned, the SBP solution was refreshed every two days to ensure a stable ion concentration in the corrosion medium. After removing the samples from the solution, the ion concentration was quantified (Fig. 11), and the pH was measured (Fig. 12). Analysis of the SBP media revealed a higher concentration of Mg^{2+} in the media where the Mg surfaces were placed after 48 h of immersion, indicating a more significant release of Mg from these samples. After 96 h, the remaining film was removed from the Si substrate. Despite the presence of Mg in the samples, its detection was not possible in the Raman spectra due to the small quantity. The pH values were correlated with the release of Mg^{2+}, with higher concentrations of this ion in the immersion fluid resulting in higher pH values.

When magnesium comes into contact with physiological fluids, it initially degrades faster due to its interaction with electrolytes. This degradation process involves the release of hydrogen ions, which subsequently leads to an increase in the pH of the surrounding medium, as dictated by the chemical reactions involved [32,60]:

$$Mg \rightarrow Mg^{2+} + 2\ e^- \text{ (anodic reaction)}$$

$$Mg^{2+} + 2\ OH^- \rightarrow Mg\ (OH)_2 \text{ (net degradation product)}$$
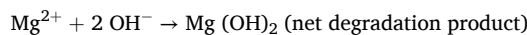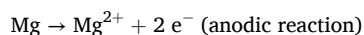
After exposing magnesium coatings to SBP, a degradation layer rich in $Mg(OH)_2$ was observed within a few hours. It is important to note that the formation of a hydroxide layer typically accompanies initial degradation and results in a temporary increase in pH. The resulting hydroxide layer is thermodynamically stable at pH values higher than 8.3, which reduces the degradation rate over time as the layer attains stability [32,60]. The recorded pH changes during the immersion tests support this hypothesis. However, a higher degree of degradation was observed when the solution was changed due to the osmolarity and lower pH value (7.4) of the fresh media. The continued degradation was caused by the formation of water-soluble $MgCl_2$ due to Cl^- ions, leading to a higher degradation rate [32,60]. SEM micrographs confirmed that after 96 h, the film was entirely degraded and dissolved (Fig. 7).

It is essential to remember that SBP, widely used in research due to its low contamination risk, has a higher content of chloride (Cl^-) ions (123 mM) than other body fluids, such as HBP (103 mM), which might hasten the degradation process [59]. Research from Heakal et al. [24] confirmed this theory by explaining that the thin layer formed during the initial phase of degradation, also known as quasi-passive, is not impervious to degradation. The resistance of the layer diminishes over time due to the aggressive attack of ions such as Cl^- or SO_4^{2-} [24,59]. These ions dissolve the passive layer, thereby reducing its protective properties.

Despite the potential of Mg as a bioactive coating for coronary stents, the outcomes demonstrated that the degradation rate of Mg during the *in vitro* tests was excessively rapid, which could impact the visualisation of the device during the healing process.

3.1.2. Zn coatings

Zinc-based materials are well-suited for medical applications due to their cellular compatibility and degradation behaviour. This study explores the potential of zinc as a coating to improve the characteristics and properties of polymeric coronary stents. This section scrutinised the degradation profile of the surface of the Zn coatings.

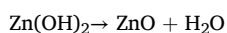Upon immersion in the SBP medium, the Zn surfaces exhibited higher degradation rates than those immersed in Milli-Q water despite
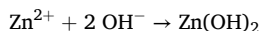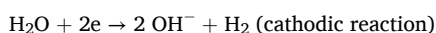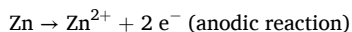
presenting a lower rate than the Mg coatings. Analysis using SEM micrographs (Fig. 7 and Figure S1 – Supplementary Information) and EDS spectra (Fig. 8) allowed for a comparison of the zinc content of the samples after 48 h of immersion in Milli-Q water and SBP. The results indicated that the zinc concentration in Milli-Q water was 39 % higher than that in SBP.

The Raman spectra (Fig. 10) also indicate some precipitates formed from degradation on the surface after 48 h of immersion in SBP, contrary to what happens in the surfaces immersed in Milli-Q water, helping explain the degradation behaviour. The presence of carbonates (~1080 cm^{-1}) and zincite (ZnO) (~430 cm^{-1}) indicates that the film is reacting with the SBP media [61]. Additionally, strong bands can be observed at around 563 cm^{-1} and 110 cm^{-1}, which are attributed to the surface optical phonon vibrations of ZnO. These bands have been detected in previous studies [55,62,63]. After prolonged immersion in SBP, additional precipitates form on the coating surfaces. These formations are identified by small peaks at approximately 981–1080 cm^{-1}, 387 cm^{-1}, and 732 cm^{-1}, which correspond to the emergence of skorpionite $[Ca_3Zn_2(PO_4)_2CO_3(OH)]$, simonkolleite $[(Zn_5Cl_2)(OH)_8]$, and hydrozincite $[Zn_5(CO_3)_2(OH)_6]$, respectively [64–67]. The SEM micrographs (Fig. 7) further confirm this observation, showing the absence of calcium and phosphate-derived degradation products after 48 h of immersion in SBP, which only appear after 96 h. Small peaks corresponding to precipitates with chloride and carbonates were also detected on the surface [61]. The micrographs of the degraded zinc surfaces also indicated the appearance of the aforementioned degradation products during the immersion period, consistent with findings from various research studies [64–67].

Regarding the Raman spectra of the surfaces that were submerged in Milli-Q water (Figure S2 – Supplementary Information), it was concluded that zinc oxide is the principal product that results from the reaction between Zn and water, which is in agreement with the Pourbaix Diagram [68]. Moreover, the EDS and SEM micrographs (Fig. 8 and Figure S1 – Supplementary Information) corroborate this evidence, illustrating the presence of Zn and O and a morphology typical wet oxidised zinc [59,69].

In order to maintain a stable ion concentration in the degradation medium, the SBP solution was refreshed at a bi-daily interval. Subsequently, the ion concentration (Fig. 11) and pH (Fig. 12) of the media were analysed. The pH measurements revealed an increase in the pH values of the Zn surfaces, attributed to the higher release of zinc ions. Following a 15-day immersion period, the zinc content in the samples immersed in SBP was determined to be 35 at.%. However, the release of zinc ions was significantly lower, a phenomenon ascribed to the chemical reaction of zinc with the inorganic components of SBP on the surfaces. This observation suggests a series of chemical reactions occurring during the degradation process. Therefore, based on the aforementioned results, the degradation mechanism of pure Zn in the SBP is associated with specific chemical reactions [64,70]:

$$Zn \rightarrow Zn^{2+} + 2\ e^-\ (anodic\ reaction)$$

$$H_2O + 2e \rightarrow 2\ OH^- + H_2\ (cathodic\ reaction)$$

$$Zn^{2+} + 2\ OH^- \rightarrow Zn(OH)_2$$

$$Zn(OH)_2 \rightarrow ZnO + H_2O$$

During immersion, zinc ions produced from the anodic reaction undergo chemical reactions with other ions in the solution. After a specific immersion period, $Zn(OH)_2$ thickens and matures, forming a precipitate on the surface. Additionally, the generation of zinc oxide catalyses the nucleation of carbonate and phosphate compounds, gradually forming a protective layer [67,70]. However, the presence of Cl^- ions poses a challenge to the growth of this protective layer. The Cl^- ions attack the protective layer, partially dissolving the degradation product [67,70].

The results also demonstrated that the degradation rates of zinc films are significantly lower than those of magnesium coatings, especially when comparing the surfaces immersed in SBP. After 48 h of immersion in physiological media, the zinc surfaces showed a higher metal content than the Mg ones. The zinc film remained intact compared to magnesium as time progressed, with the Zn content around 37 at.% after 96 h. Even after 15 days of immersion, the zinc content was 35 at.%. In contrast, the samples coated with magnesium showed no traces of magnesium. When immersed in MilliQ water, Zn surfaces demonstrated even higher concentration values than the Mg coatings subjected to the same conditions.

Several studies have indicated that the standard potential (E^0) is a key indicator of the chemical reactivity of magnesium and zinc and, consequently, their degradation behaviour [71,72]. According to the literature, a negative potential signifies an active potential, and the lower the value, the more susceptible the metal is to corrosion. The E^0 of magnesium is -2.37 V. At the same time, for zinc, it is approximately -0.44 V, indicating that pure magnesium is more reactive than zinc and undergoes oxidation more rapidly in aqueous media [73–75]. Another significant consideration is the presence of complexing agents that displace water molecules in the hydration of dissolved ion metals (Mg^{2+} and Zn^{2+}). These ligands alter the stoichiometry of the metal dissolution reaction, typically resulting in a lower standard potential. For instance, the ion Cl^- acts as a complexing agent. The equilibrium constant of a complex formation between a metallic ion and the dissolved complexing agent can be determined using Nernst equations [73].

Multiple studies have indicated that Mg and Zn are suitable materials for coronary stents [23,76,77]. The objective of the study was to use these materials as coatings to improve bioresorbable polymeric-based stents. Both coatings were observed to degrade in a blood-like liquid, making them suitable for biodegradable stents. However, the Mg coatings degrade too quickly. Thus, zinc outperforms Mg as it is more resistant to degradation over time. The degradation rate of Zn films will facilitate the release of zinc during the healing process after the implantation of a coronary stent, enabling proper therapeutic treatment of the arteries and visualisation of the medical device [20]. As the second most abundant trace metal in the human body, zinc can be found in all organs, tissues, fluids, and secretions. Unlike other metals, such as iron, zinc exists as Zn^{2+} in a free form that does not trigger redox reactions in physiological conditions, making it a relatively non-toxic substance [78]. Based on these properties, it can be inferred that a zinc coating deposited at 0.4 Pa is a promising candidate for functionalising a polymeric BRS.

3.2. Antibacterial tests

In medical settings, patients undergoing treatment are vulnerable to acquiring nosocomial infections unrelated to their medical conditions. One emerging concern is implant-associated bacterial infections, which have imposed significant economic burdens on medical resources and inflicted additional suffering on patients. Bacteria can tightly adhere to biomaterial surfaces, forming a protective biofilm, making it difficult to treat infections and leading to implantation failures. The overuse of antibiotics has contributed to an increase in antibiotic-resistant bacteria, underscoring the urgent need for materials with strong antibacterial properties [37]. Although infectious complications following percutaneous cardiac interventions are uncommon, coronary stent implantation can lead to rare complications such as stent infection. It is essential to be mindful of these possibilities and take preventive measures [79]. If complications do arise, they necessitate special investigations for diagnosis and management. While most reported cases have had unfavourable outcomes requiring surgical treatment, interventional cardiologists should be prepared to address these potential complications [80]. Coronary stent infection is associated with an in-hospital mortality rate of up to 30.3 %. *S. aureus* is the most common organism during the first days of implantation in 65 % of cases, of which 21.9 %

are methicillin-resistant. Thus, coronary stent infections represent a highly fatal yet potentially preventable problem of PCI [38].

One strategy to avoid bacterial adhesion and proliferation involves modifying surfaces. In this context, coatings containing magnesium and zinc have been identified as effective in inhibiting bacterial growth and fungal activity [79]. The antibacterial properties of these coatings were tested against three common types of bacteria found in medical facilities and in patients who have undergone coronary stent procedures: *S. aureus*, *P. aeruginosa*, and *E. coli* [38]. Fig. 13 shows the bacterial viability results for cells exposed to Mg and Zn coatings, compared to the uncoating control, and Table 5 presents the antibacterial efficiency.

PLA and PCL, members of the aliphatic polyester family, are commonly used as biodegradable polymers in the structure of coronary stents. Despite demonstrating reasonable mechanical properties [2], the literature indicates these polymers lack antibacterial properties [81,82]. As of the writing of this manuscript, no studies have been found utilising pure Mg and Zn as coatings for polymeric coronary stents or examining their influence on antimicrobial activity. However, some studies have shown positive effects in inhibiting the growth and proliferation of Gram+ and Gram− bacterial strains when using composite structures with the proposed polymeric and metallic materials. It is important to note that most studies have used oxide particles to reinforce the polymeric matrix and not the pure metallic elements [83–85].

In Fig. 13, it is evident that there is a statistically significant decrease in the presence of bacteria on the surfaces after the modification of the polymeric materials. The antibacterial effectiveness is particularly notable against *E.coli* and *S. aureus*, two common organisms responsible for infections in the early stages of coronary stent implantation, with an antibacterial efficiency ranging from 92 % to 100 %. This highlights the advantages of using metallic coatings to reduce infections following the placement of a coronary stent. Furthermore, the antibacterial efficiency against *P. aeruginosa*, a Gram− bacteria known for its antibiotic multi-resistance, is over 50 %, particularly for the polymers coated with Zn. The literature indicated that numerous scientists have proposed several

Table 5

Antibacterial efficiency of the tested surfaces against *S. aureus*, *P. aeruginosa* and *E. coli* strains.

Surface	CFU (x10³)			Antibacterial Efficiency (%)		
	S. aureus	E. coli	P. aeruginosa	S. aureus	E. coli	P. aeruginosa
PLA	38 ± 7	24 ± 3	447 ± 48			
PLA + Mg	3 ± 2	0 ± 0	172 ± 29	92	100	62
PLA + Zn	0 ± 0	0 ± 0	11 ± 7	100	100	98
PCL	47 ± 11	39 ± 6	457 ± 48			
PCL + Mg	1 ± 1	4 ± 4	230 ± 39	98	90	50
PCL + Zn	1 ± 1	3 ± 3	115 ± 25	99	92	75

potential bactericidal mechanisms of Mg and Zn that hinder the growth of these strains [86,87]. Fig. 14 illustrates a schematic representation of possible antibacterial mechanisms due to the presence of Zn and Mg ions, according to the descriptions reported in the literature [86,87] and must be interpreted only as a visual aid.

Magnesium corrodes rapidly under normal physiological conditions with high chloride concentration and a pH between 7.4 and 7.6. This corrosion increases pH value and Mg^{2+} concentrations, inhibiting the growth of *E. coli*, *P. aeruginosa*, and *S. aureus* strains. The potential of Mg ions as an antibacterial agent is intriguing. Studies have shown that high concentrations of Mg ions could prevent bacteria adhesion and biofilm formation, making bacterial cells more vulnerable to adverse conditions and antibacterial agents [79]. Published research has indicated that higher Mg^{2+} concentrations result in a stronger antibacterial effect, likely due to increased osmotic stress on the cell wall [88]. Additionally, Mg^{2+} ions were effective against *S. aureus*, potentially disrupting
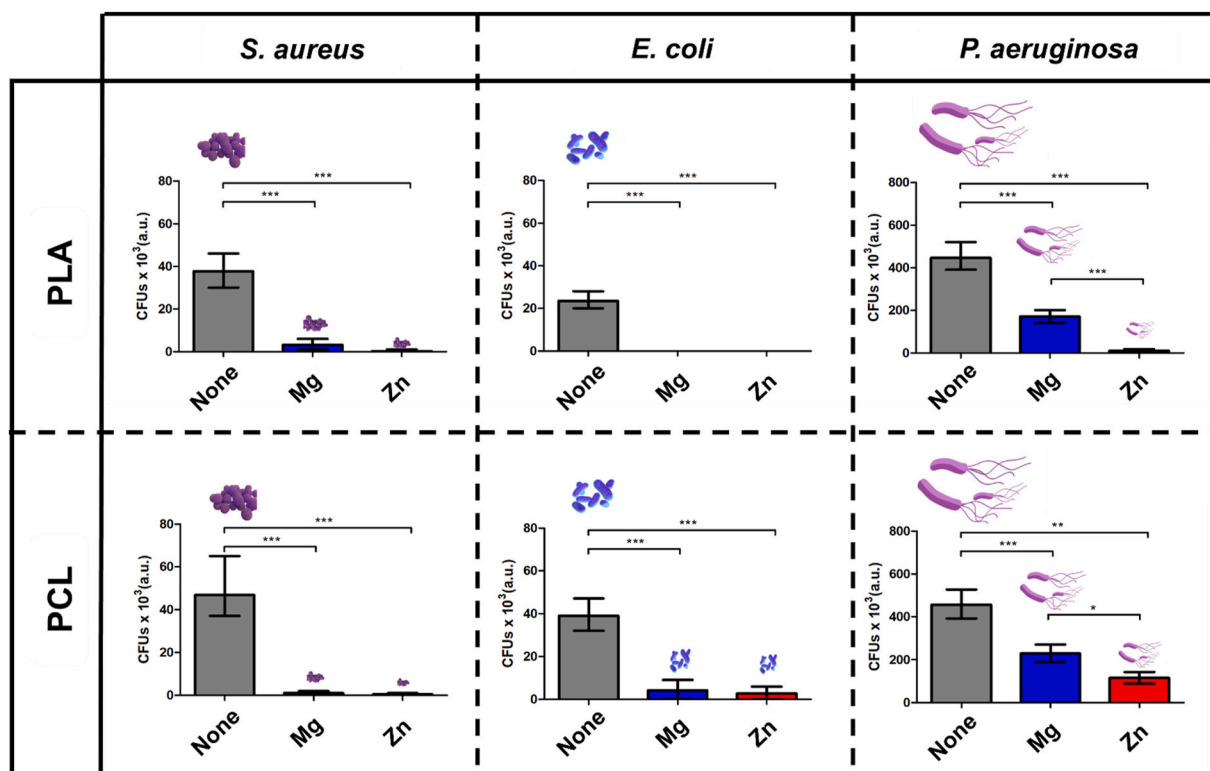
Fig. 13. Quantitative analysis of viable bacteria on the surface of the polymers, coated and uncoated, after 24 h of incubation at 37°C, determined by the spread plate method.
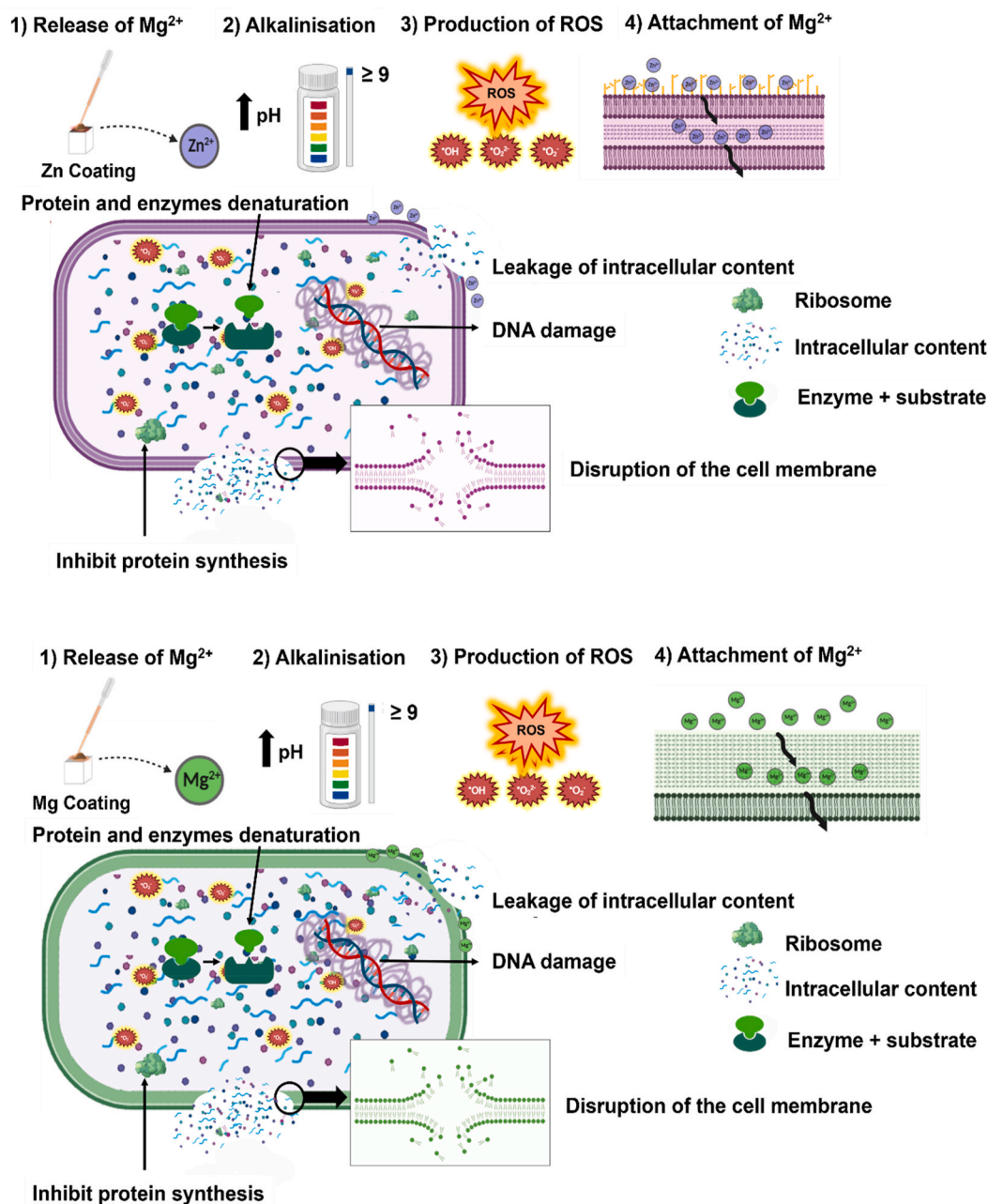
Fig. 14. Schematic representation of possible antibacterial mechanisms for Zn and Mg ions, according to the literature descriptions (Created in BioRender.com).

bacterial membranes [88]. However, other studies suggest that the antibacterial properties of Mg are independent of Mg ions and may be influenced by the alkaline environment [86]. The intracellular concentration of Mg in many cell types is relatively high, ranging between 15 mM and 30 mM. Therefore, when Mg ions are used alone as an antibacterial agent, their concentration must exceed the one inside bacterial cells. However, when combined with an alkaline environment, even a moderate concentration of Mg^{2+} can yield a strong antibacterial effect [79]. At the same time, corrosion product $Mg(OH)_2$ precipitates demonstrated little contribution to the antibacterial properties of Mg-based materials due to their easy transformation into soluble $MgCl_2$ [89,90].

In the present study, Mg ions were rapidly released after 48 h, reaching a concentration of around 21 mg mL^{-1} (868 mM) into the media. This rapid release is notable, as it is a concentration enough to kill most bacteria [91,92]. The pH value also increased, and the film was almost degraded after 24 h of incubation with the bacteria strains. The higher concentration of Mg^{2+} ions can lead to cellular enzyme deactivation, resulting in increased levels of reactive oxygen species (ROS). Bacteria produce enzymes such as superoxide dismutase, catalase, or proteins like thioredoxin to neutralise the generated ROS as a defence mechanism. Nonetheless, in the presence of Mg ions, an excess amount of ROS can be produced, overwhelming the defence mechanisms of the bacteria and causing oxidative stress, ultimately leading to cell necrosis [91,92].

Another non-ROS antibacterial mechanism might involve cellular membrane damage. Due to the positive surface charge of the ions, they bind electrostatically to the cell membrane of bacteria (negative charge), leading to membrane distortion, cytoplasmic material leakage, and, ultimately, cell death [91,92].

Within the metallic coatings, zinc was more effective against the tested bacteria, particularly against the *P. aeruginosa* strain. Literature reports that zinc-based materials have a lower minimal inhibitory concentration (MIC) than magnesium-based materials. For example, concentrations of zinc higher than 1 mM and 10 mM in the physiological medium can inhibit the growth of *P. aeruginosa* and *S. aureus* strains, respectively, which is a lower value than those observed for magnesium-based materials [37]. The concentration of Zn^{2+} after 48 h was around 9.5 mg per mL (144 mM), sufficient to inhibit cell proliferation post-implantation and increase pH values. The antibacterial mechanism of zinc involves the oxidation of water molecules or hydroxide anions in bodily fluids [64,70]. This oxidation mechanism leads to a chain reaction resulting in the production of ROS that have bactericidal effects. The stress resulting from ROS production can impact the structure of bacterial membranes, leading to the loss of their selective function.

Furthermore, the energy production and DNA replication of bacteria can be affected by ROS [87]. Zn^{2+} can bind to the surfaces of Gram+ and Gram− bacteria through various metabolic pathways, ultimately damaging the cell surface. Zinc-based materials have multi-target compounds, affecting several structures of bacterial cells, but their primary mechanism of action is on the cytoplasmic membrane, with other structural effects occurring as a consequence [93] (Fig. 14).

The antibacterial analysis affirms the efficacy of both coatings in reducing the proliferation of prevalent bacterial strains in the medical sector, thereby averting post-implantation infections following coronary stent procedures.

3.3. Blood clotting assays

One common occurrence after stent implantation is in-stent thrombosis (IST), caused by the formation of blood clots. In fact, in cases involving this device, IST can lead to myocardial infarction and mortality in up to 80 % of cases [94]. The main causes are damage to the artery lining, lack of anti-clotting substances, plaque rupture, stent design, or the materials used.

When implanted, the device and its materials evoke a healing response from the body, and the goal is seamless integration without triggering chronic inflammation that could lead to implant failure. Upon contact with the tissues of the body, proteins in the blood and interstitial fluids adhere to the surface of the biomaterial, regulating clotting, immune response, and inflammation.

Factors such as Factor XII and Factor VII, as well as the activation and adhesion of platelets, can contribute to clot formation. Furthermore, the biomaterial surface can activate the complement system, which is associated with an immune response [94–96] as schematically represented in Fig. 15 that serves as a visual aid using information from the literature. Hence, it is essential to engineer biomaterials that discourage coagulation and inflammation to facilitate successful bodily integration.

In this section, we will focus on how materials can influence blood clot formation, which can be due to foreign material contact or hypersensitivity reactions to the corrosion products. The activation of the contact pathway of coagulation was evaluated by using static *in vitro* blood clotting assays to measure the thrombogenicity (%) (Fig. 16) and BCI (%) (Fig. 17) of both the coated and uncoated polymers.

Polymeric materials such as PLA and PCL have been extensively studied for their interface with the human body. Although the results of this study showed that thrombosis and BCI occur more frequently in bare polymers than in coated samples, several researchers have noted that bioresorbable polymeric materials have a lower likelihood of thrombus formation than permanent metallic stents like CoCr [4]. Both bioresorbable polymeric materials are FDA-approved as part of stents, specifically as coatings for drug-eluting stents made with CoCr, due to their ability to reduce the thrombogenic effect. The use of these biodegradable polymers as coatings has demonstrated excellent results [4]. In the case of polymeric frameworks, most thrombosis occurrences are attributed to the greater thickness of the strut and blood flow disturbances, which could potentially lead to blood clot formation rather than the material itself [4,97]. Nevertheless, initiating dual antiplatelet therapy is always necessary to prevent stent thrombosis, which may explain the outcomes of the current study [98].

Considering the potential for blood clot formation, the research outcomes indicated that the uncoated polymeric samples and the specimens coated with magnesium developed a clot within the stipulated time. Additionally, the magnesium coating fully degraded upon contact with the blood sample. Compared to the *in vitro* degradation tests (section 3.1), the degradation of the coatings in whole blood occurs significantly faster. Recognising that the dynamics observed in biological or *in vivo* samples differ from SBP is important. In this context, it is crucial to
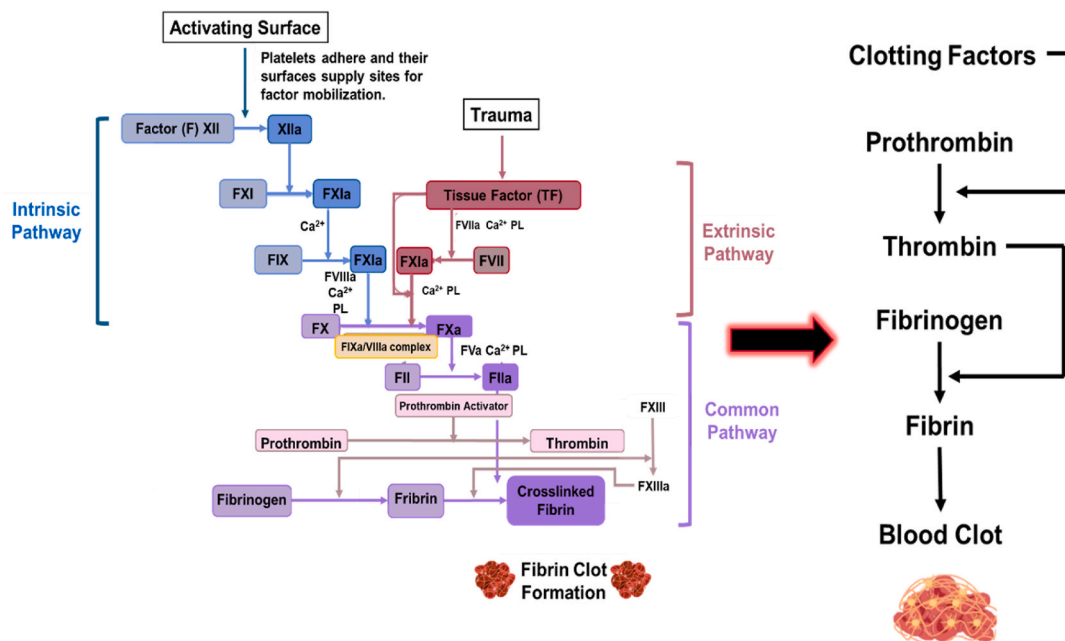

Fig. 15. Schematic representation of thrombus formation: A simplified diagram of the blood coagulation cascade and thrombus formation resulting from the activation of the intrinsic, extrinsic, and common pathways according to literature information (Created in BioRender.com).
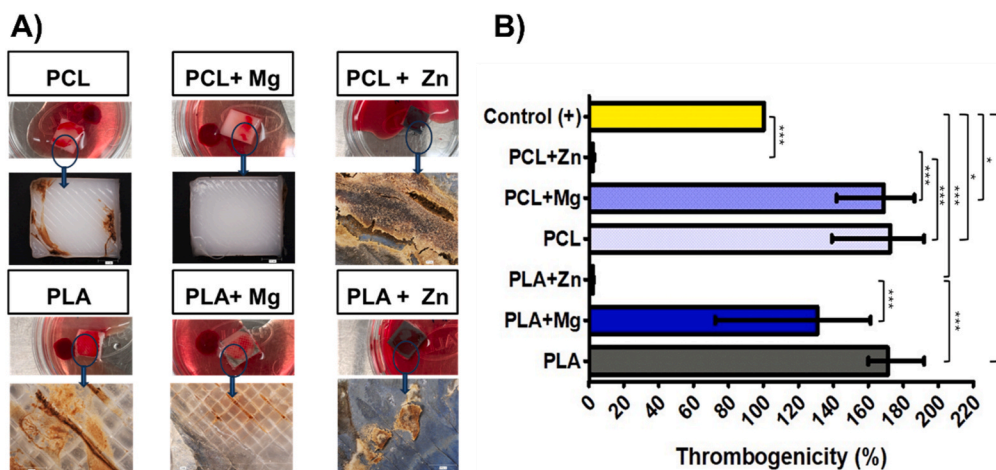
Fig. 16. Thrombus formation during the static *in vitro* blood clotting assays: A) Representative images of the blood clot after incubation; B) Thrombogenicity percentage of the tested samples.
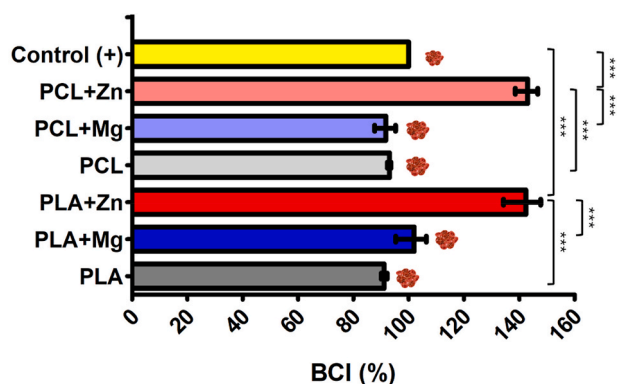

Fig. 17. Blood Clotting Index of all tested surfaces.

consider the influence of organic components on the degradation of the coatings, including, for instance, proteins or platelets [99]. For example, approximately 55 % of blood proteins consist of serum albumin, with average concentrations typically ranging from 30 to 50 g L^{-1} [24]. Existing literature suggests that within this concentration range, the degradation rate of magnesium may be enhanced due to protein aggregation, thereby accelerating the overall process [24].

Regarding the blood clotting index, this parameter measures the amount of Hb released from haemolysed red blood cells that were not incorporated into the clots formed. Higher absorbance of haemoglobin indicates a higher clotting index [41] and, consequently, a lower clotting rate. According to the results, samples coated with magnesium also demonstrated a higher probability of forming thrombi on their surface than zinc. Although the findings suggest a minor decrease in thrombus formation and lower BCI in samples coated with Mg, the difference was not considered significant compared to the uncoated polymeric substrates.

Despite previous indications of antithrombotic properties in materials based on Mg [79], the presence of a clot was observed in this work. This occurrence of thrombus formation can be attributed to the rapid degradation of the metallic coating upon contact with whole blood [100]. Adverse reactions resulting from rapid degradation, such as an increase in Mg^{2+} or local alkalisation, lead to the rapid generation of substantial amounts of hydrogen, causing side effects that promote the activation of the blood cascade [100]. A study by Pan et al. [101] noted that platelets adhere more to the surface of magnesium implants when there is a higher degradation rate. The authors described that the fast degradation of the magnesium alloy in the physiological environment,

combined with a rapid increase in pH value, significantly impacted red blood cells and the rate of haemolysis. They also noticed a shorter clotting time than other materials, indicating quicker clot formation [101]. Another study by Zhen and colleagues [102] explained that when the concentration of Mg^{2+} reaches 1 mg mL^{-1}, there is a minimal destructive effect on erythrocytes, and the high pH value is the primary reason for the high haemolysis ratio and thrombus formation. These findings help to explain the results since it was confirmed that the film degraded at a very high rate, leading to its almost complete degradation, as shown in Fig. 16A [102].

Considering the surfaces coated with Zn, there is a notable decrease in thrombogenicity percentage and an increase in BCI compared to the remaining samples and the positive control. Additionally, the zinc-coated samples did not degrade during the incubation period, and the blood clotting index measurements also showed that the polymers coated with zinc are the least likely to form thrombi on their surface. These findings agree with published works indicating that zinc-based materials lead to lower platelet activation and haemolysis rates, resulting in reduced thrombogenicity percentage [23,103]. Platelet activation encompasses various phases, such as platelet deformations, adhesion, aggregation, and release reactions, including the liberation of various factors [104]. According to a study by Tamura et al. [105], zinc can offer protective effects by promoting the production of nitric oxide (NO), which is known to have various physiological activities, including inhibiting platelet aggregation and, thus, minimising the probability of thrombus formation. Furthermore, Yue and colleagues [104] demonstrated that zinc yields low platelet adhesion, implying no adverse effect on thrombogenicity. Additionally, the gradual release of zinc over time may be advantageous in reducing the probability of developing other cardiovascular diseases. It has been proven that higher serum zinc levels are connected to a lower risk of myocardial infarction [105]. Fig. 18 presents a simplified schematic representation that illustrates the information of the previously discussed theories about the presence/absence of thrombus in response to the degradation of Mg and Zn in whole blood, according to the literature [23,100–105].

CoCr alloys used in coronary stents in the medical field have been found to trigger blood clotting and inflammation due to their ability to activate platelets, coagulation, and induce white blood cell adhesion. These factors can lead to IST when the stents are implanted without a polymeric coating and pharmaceuticals [106]. In the present study, the coated samples, especially those coated with zinc, show promising outcomes as they have a lower tendency for thrombus formation. This is consistent with findings from a study by Anderson et al. [107], which compared various metallic materials for stent application and found that Fe, molybdenum (Mo), 316L SS, CoCr, and nickel-titanium (NiTi) had
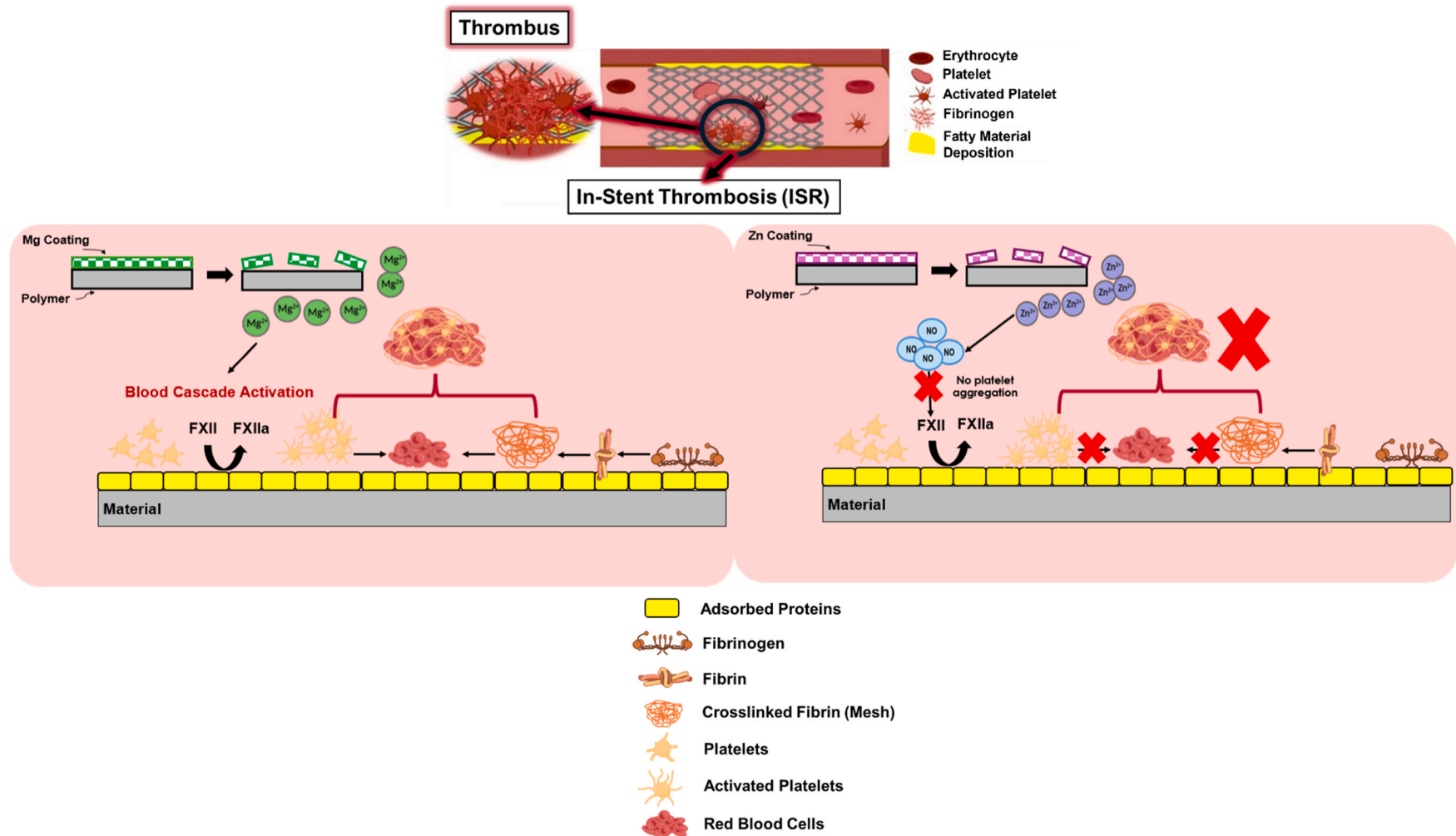
Fig. 18. A simplified schematic representation that illustrates a possible explanation of the thrombus formation occurring on the material surfaces through the activation of coagulation factors (such as, fibrinogen, FXIIa) adsorbed to the materials (Created in BioRender.com).

significantly higher FXIIa generation rates compared to Mg and Zn, indicating a higher prospect of blood cascade activation and, consequently, thrombus formation [107].

The findings exposed in this section indicate that Zn-coated polymers may possess inherent anticoagulant properties due to the absence of a thrombus on the surface of the samples. Some researchers have already demonstrated that creating coatings with anticoagulant properties is possible. They indicated the potential to lower the concentration of pharmaceuticals applied to the stents or even develop drug-free stents [108–110]. In this context, Zn coating is a novelty for highly functional coatings that can enhance the performance of polymeric-based stents concerning in-stent thrombosis and other related properties.

3.4. Radiopacity

One of the critical aspects of the stenting procedure is the precise positioning and deployment of stents, which is carried out by interventional cardiologists using medical imaging techniques. The literature defines radiopacity as the ability of a material to absorb radiation and appear in white or opaque medical images, such as on radiographs. Radiopacity can be assessed by qualitatively comparing images or quantitatively determining the specific difference in optical density or pixel intensity between the test specimen and the standard [43].

According to previous works [111], one of the methods to evaluate quantitatively the radiopacity is dependent on the X-ray attenuation caused by the stent material and is characterised by a parameter known as the linear attenuation coefficient (μ) (cm^{-1}). Attenuation refers to the reduction in the intensity of an X-ray beam as it passes through a material due to the absorption or scattering of photons from the beam, and it is calculated according to equations (4) and (5), in which x is the mass thickness (calculated by multiplying the thickness by the density), $I_{incident}$ and $I_{transmitted}$ are the intensities of the incident and transmitted beams, respectively.

$$Radiopacity = \frac{I_{incident}}{I_{transmitted}} \qquad \text{Equation 4}$$

$$\frac{I_{incident}}{I_{transmitted}} = \exp\left[-\mu\,x\right] \qquad \text{Equation 5}$$

Another reliable method for evaluating radiopacity from CT images is using the Hounsfield scale. This scale measures the attenuation value of the radiation in a specific voxel and compares it to the attenuation of water [112]. CT attenuation values are indicated in Hounsfield units (HU), named after Sir Godfrey Newbold Hounsfield, the pioneer of CT scanning. The HU values of each pixel undergo digital image conversion by assigning a grayscale intensity to each value. Higher values indicate increased pixel brightness, meaning an increased radiation absorption [113–115]. Additionally, the HU is directly correlated to the μ value of the sample at a specific energy level of the CT scanner, where μ_w is the linear attenuation coefficient of the water (Equation (6)) [116]. The μ_w for the equipment used in this study was considered 0.35 cm^{-1}.

$$HU = \frac{\mu_{sample} - \mu_w}{\mu_w} \times 1000 \qquad \text{Equation 6}$$

Remember that these evaluation methods rely on the grayscale values (GSV) of each pixel, which range from 0 to 255. A value of 0 represents the darkest shade, while 255 is the brightest. Thus, materials with higher μ and HU will have a pixel value of around 255, making them visible in the medical image. According to previous studies in the field, equation (7) gives the percentage of contrast of the coated samples relative to the uncoated polymers [117].

$$Contrast\ (\%) = \frac{GSV_{coated} - GSV_{uncoated}}{GSV_{coated} + GSV_{uncoated}} \times 100 \qquad \text{Equation 7}$$

The qualitative analysis involved evaluating the 3D projections of images of the coated samples compared to the uncoated polymer, from

which the contrast results were extracted (Fig. 19). The quantitative analysis of radiopacity was carried out by calculating the HU values and the linear attenuation coefficients (Fig. 20).

The literature shows that a material should be composed of elements with higher density and higher attenuation coefficients to enhance the visibility of stents in medical imaging [111]. One proposed material as the base structure for coronary stents is 316L SS, but it demonstrated poor visibility with a linear attenuation coefficient of 2.91 cm^{-1}. CoCr alloy-based stents have become recently the gold standard in this medical field due to their improved radiopacity (μ = 7.33 cm^{-1}) [111]. However, as discussed previously, these stents have many adverse issues, such as their permanent metallic structure, which can trigger biological events over time. Bioresorbable stents have been developed to reduce the occurrence of these biological events since they are degradable over time.

In this context, certain studies have proposed the addition of radiopaque markers, but these markers still have limited dissolution in the human body [6]. Other researchers have proposed blending polymeric materials with other compounds to increase radiopacity. For instance, Wang and colleagues [118] suggested adding iohexol particles to the polymeric matrix to achieve higher radiopacity. However, although this procedure improved radiopacity, it also decreased the mechanical properties [118]. Another study by Srivaskava et al. [31] suggested blending PLA/PCL/Mg-Zn-Y to improve radiopacity, but elements such as yttrium (Y) are known to be genotoxic and cytotoxic [119]. Recent studies have indicated the use of radiopaque surface coatings, such as gold, to improve the traceability and precise positioning of stents made with materials with lower attenuation values [30]. However, clinical studies have found that gold coatings may increase the risk of biological events following stent implantation [111].

The materials used in this study are both degradable when in contact with bodily fluids, which is an improvement compared to previous studies that used coatings to enhance radiopacity. The results show that zinc has significantly higher radiopacity values than magnesium. The qualitative analysis of contrast percentage compared to the polymeric control also indicated a noticeable difference. This observation can be attributed to the higher thickness of the Zn film and its atomic number. According to Stinson and colleagues [120,121], an effective atomic number (Z) greater than 22 is the minimum requirement for a material to impart radiopacity. This explains why the magnesium film does not provide higher visibility during tomography analysis compared to the zinc coating, which shows better coating distribution, a more compact and dense film, and higher values of linear attenuation coefficient and HU. The same work specifies that radiopaque markers should have a minimum linear attenuation coefficient of 5.46 cm^{-1} with a thickness of less than 10 μm [120,121]. The zinc coating provides a μ = 6.2 ± 0.4 cm^{-1}, which surpasses the desired value for ensuring good radiopacity [121]. On the other hand, the magnesium coating has values similar to those of HU and a linear attenuation coefficient compared to the polymeric material, which is insufficient to accomplish the requested radiopacity.

Hence, the deposition of a zinc coating offers a practical solution for improving radiopacity and reducing post-implantation complications such as thrombosis. Additionally, magnetic resonance imaging (MRI) can be used as an alternative to CT to monitor stent placement. Zinc, with MRI compatibility similar to polymers and ceramics, is a promising choice for coating biodegradable stents, as it is MRI-compatible, unlike CoCr stents, which can cause imaging artefacts [103].

3.5. Mechanical characterisation

3.5.1. Tensile test

When evaluating coronary stents, it is crucial to ensure adequate plastic deformation during expansion to prevent elastic recoil [2]. Following the selection of an adequate design as recommended by the literature [2], the 2D geometry of the stents was printed and coated with
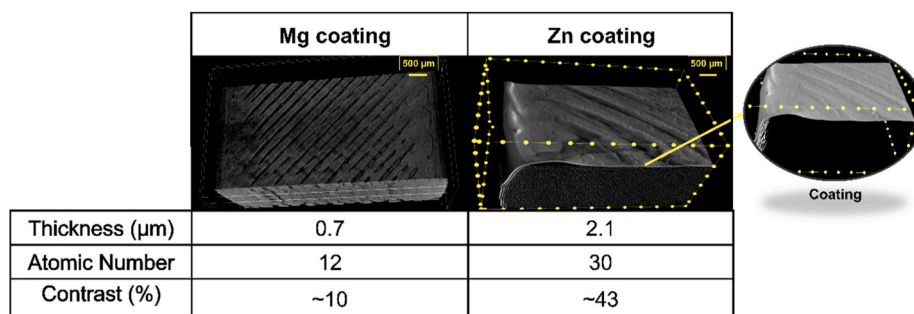
Fig. 19. Representative Images of the micro-CT analysis of the coated polymers, displaying the thickness of the coatings, the atomic number of the metallic elements and % of contrast increase in relation with the polymer.
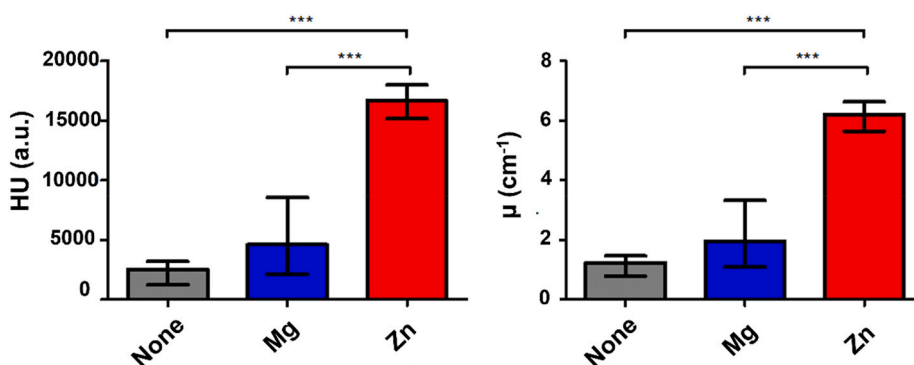

Fig. 20. Quantitative analysis of radiopacity.

metallic films. Characterisation was made through tensile tests to evaluate the influence of the coatings on the behaviour of the stent, particularly on yield strength [111,122]. Additionally, the study examined the adhesion of the coatings to the polymers during stent expansion. This evaluation was achieved by observing the morphology of the stents post-test and gauging the electrical resistance during the tensile test. Additionally, the study investigated how well the coatings adhered to the polymers during stent expansion since the literature reports that delamination of the coating from the substrate during intravascular deployment is common and can lead to adverse patient outcomes [123]. This evaluation was achieved by observing the stents post-test and gauging the electrical resistance during the tensile test. A limit of 5 % strain of the stent was applied for this test. Stress was measured in kPa as recommended by ISO standard 25539-2. Fig. 21 illustrates representative stress (σ) vs. strain (ε) curves obtained during the mechanical tests. Fig. 22 presents the yield strength (σ_y) values (mean $\pm$ SD) of the uncoated and coated stents.

Stent expansion is the result of compressive and tensile forces, with the former primarily influenced by vessel characteristics such as wall stiffness and plaque morphology and the latter dependent on the applied pressure, deployment time, and properties/characteristics of the stent, including strut design and material [124]. An essential consideration for stents is the yield strength of the materials, which generates multifaceted outcomes. While higher yield strength can improve stent performance by enhancing radial strength, it can also increase recoil and reduce flexibility during deployment, consequently jeopardising the stent performance [111,122].

Since polymeric materials are known for having viscoelastic properties, lower yield stress is preferred to ensure that plastic deformation occurs [111,122,125–127]. The deformation must be enough to prevent displacement after implantation but without subjecting the stent to excessive load, which could otherwise lead to higher stress in the artery and potential restenosis due to endothelial damage [124]. According to this research (Fig. 22), when stents are coated with metal, they may
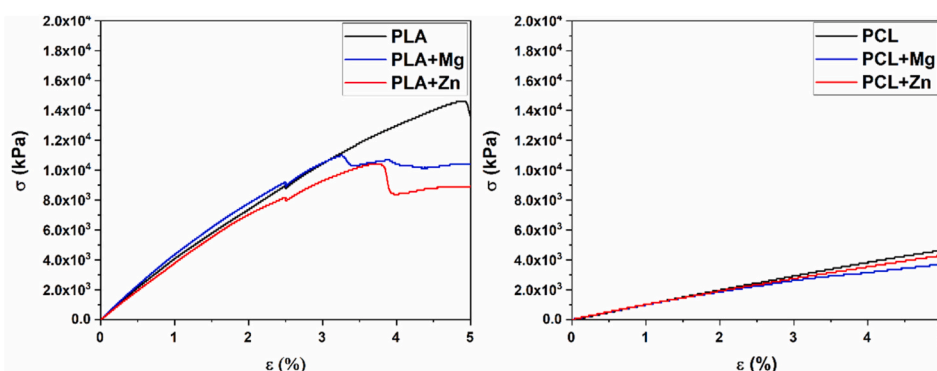

Fig. 21. Representative stress-strain curves of the uncoated and coated stents.
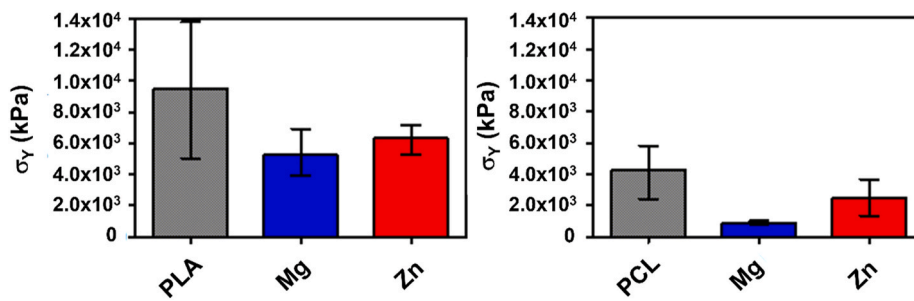
Fig. 22. Yield strength (mean $\pm$ SD) of the uncoated and coated stents.

experience a reduction in yield strength. This implies that the modified stents can undergo a higher level of plastic deformation for the same displacement, resulting in a lower recoil ratio.

Moreover, the experimental mechanical tests indicated that PLA-based stents have higher yield strength than PCL but they also have a higher probability of fracture during tensile test, as shown in Fig. 21. These results align with former computational analyses indicating that PLA-based stents are more likely to fracture during expansion with a balloon [2].

Compared to the clinical benchmark CoCr, the yield strength values for all material configurations presented in this work are lower [128]. However, polymer-based stents necessitate lower balloon pressures for deployment, which reduces the risk of thrombosis and restenosis by imposing lower stresses on the artery system than permanent metallic stents. Additionally, there is less property mismatch between polymers and arterial tissues, potentially offering clinical benefits [128]. Although metallic coatings were used in this work, they are beneficial for coating coronary stents as they lower the probability of thrombus formation, reducing the percentage of thrombosis, as previously demonstrated in section 3.3.

Numerous medical papers have documented the stent coating becoming detached from the substrate during artery placement, leading to adverse patient outcomes. This is attributed to the differing properties of the metallic and polymeric materials, as well as the minimal thickness of the coating, which experiences substantial plastic strains during deployment compared to the base structure [123]. As widely documented in the literature, polymeric materials are known for being electric insulators with no conductivity [129]. In contrast, metals exhibit lower resistance and higher conductance than polymeric materials. Consequently, the electrical conductance of the stent designs can be enhanced by using metallic coatings.

According to the literature, it is possible to confirm the detachment of a metallic coating from a non-conductive polymeric substrate by evaluating its electrical properties [130]. A fully adhered conductive coating maintains the overall electrical pathway, while a coating detachment, whether due to delamination, cracking, or other occurrences, disrupts the pathway and leads to changes in electrical conductivity or resistance [130,131]. This fundamental principle can be leveraged to detect detachment or delamination of the metallic coating.

The evaluation of film adhesion involved measuring the electrical conductance of the stent design during a tensile test by maintaining a 20 mm distance between the clamp electrodes, and these placed in contact with the coated samples. During the strain, the electrical resistance was measured. By disregarding minor changes in the intrinsic conduction of materials and focusing on the geometric effect caused by the applied strain, it is possible to quantify the normalised electrical resistance behaviour using Equation (8). In this equation, R_0 represents the initial electrical resistance before the strain, R denotes the measured electrical resistance during the strain, L_0 is the initial gauge length, and L is the gauge length during the test [130,132].

$$\frac{R}{R_0} = \left(\frac{L}{L_0}\right)^2 = (1 + \varepsilon)^2 \qquad \text{Equation 8}$$

The electrical conductance was calculated using Equation (9), where $R_{Normalised}$ is the resistance value after normalisation [133].

$$Electrical\ Conductance = \frac{1}{R_{Normalised}} \qquad \text{Equation 9}$$

The electrical conductance of the surface-modified polymeric stents was assessed to anticipate any alterations during expansion and to detect potential coating detachment (Fig. 23). Moreover, optical images of the stent design post-test were captured, and the specimens were examined under an optical microscope (Fig. 24).

The main purpose of this experimental test was to compare the electrical properties of different polymeric materials coated with two metallic coatings. Analysis of the results reveals the absence of significant alterations in electrical properties during the tensile test, signifying no coating detachment for the specified strain. Furthermore, macroscopic optical images confirm the lack of discernible cracks in areas predisposed to fracturing during the tensile test. Prior research findings suggest that the higher stress and potential for fracturing during PCI occur at the strut connections and curved regions during stent expansion [134,135]. Thus, an induced fracture in these high-stress areas conclusively demonstrates the sustained adhesion of the film to the substrate under these conditions (inset in Fig. 24). Notably, despite the minimal thickness of the coatings, the induced strain during the tensile test does not compromise their adhesion to the polymeric substrate. This observation strongly suggests that there will be no detachment during the PCI.

According to the literature survey, no reported studies have specifically investigated the application of this method for assessing the detachment of a coating from a coronary stent. The outcomes of this study and prospective considerations concerning responsive stents indicate that this approach could prove valuable in identifying potential shortcomings during stent deployment. Certain studies have suggested the feasibility of utilising a balloon equipped with electrodes to ascertain the electrical conductivity of the stents during their expansion [136, 137]. Integrating these technologies can enhance the accuracy of stent placement, thus predicting and reducing the risk of procedural misalignment that may lead to post-stenting biological events.

3.5.2. Cyclic compression

The compression tests were carried out by the recommendations outlined in the literature and the ISO standard 25539-2 [47,48,138]. This standard specifies that the compression tests are intended to "*evaluate the long-term structural integrity of the stent when subjected to cyclic compressive loading perpendicular to the stent axis, which is appropriate for the device design and intended clinical application*" [47]. According to ISO standard 25539-2, the normalised force was calculated for each configuration, considering the length of the coronary stent [47]. Fig. 25 illustrates the values of the maximum normalised compressive force (mean $\pm$ SD) during the cyclic tests.

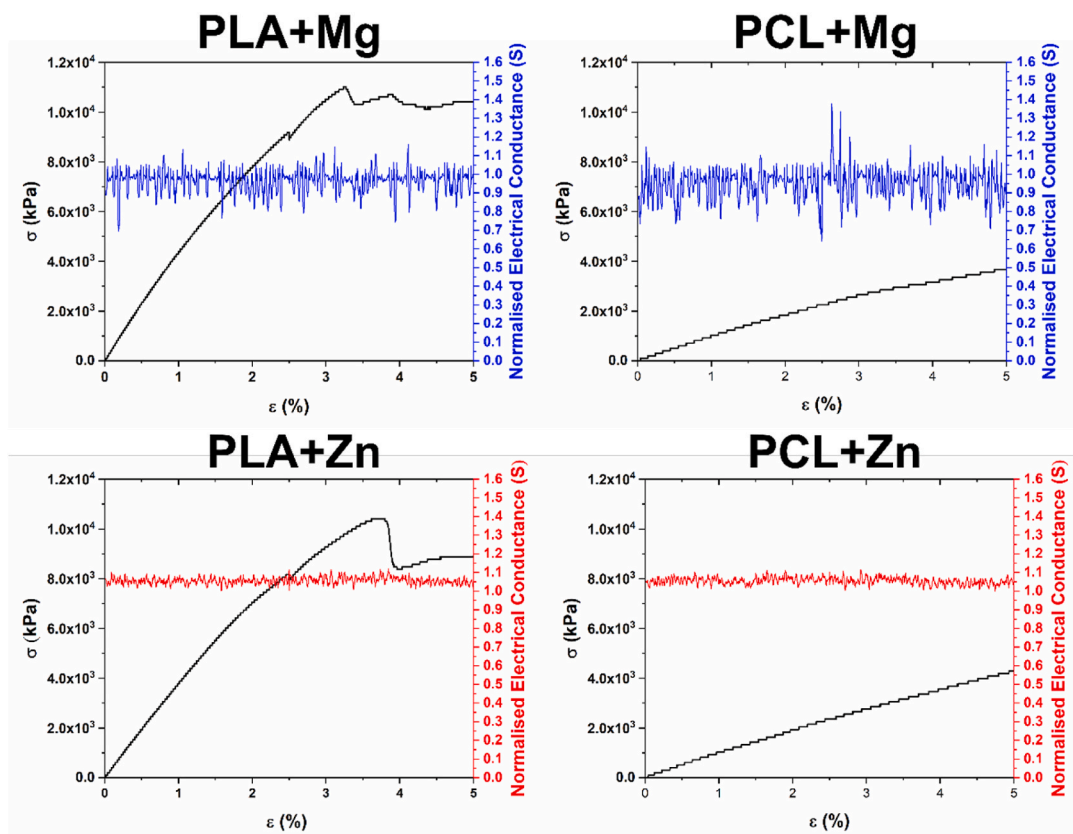The research found that stents with surface modifications

Fig. 23. Representative stress-strain curves and normalised electrical conductance of the coated stents during the tensile tests.
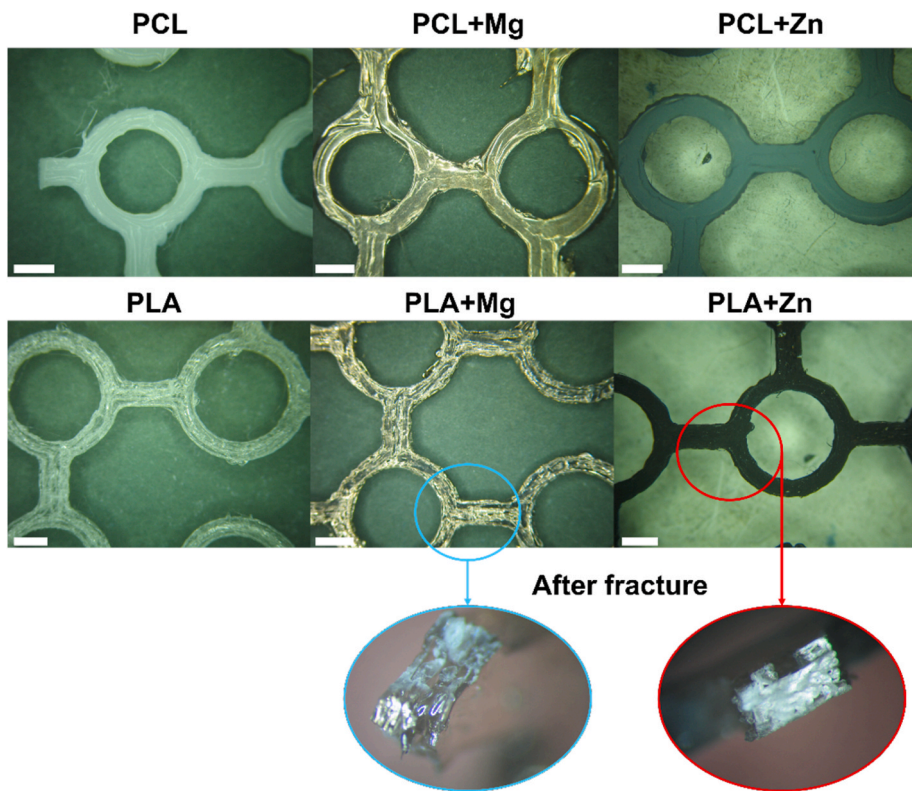

Fig. 24. Representative optical images of stents after a tensile test (inset following the tensile test, an induced section was fractured to observe if the coating remained attached to the polymeric substrate) (bar = 2 mm).

demonstrate increased strength when subjected to compressive loading conditions, especially PCL-based stents. Considering only the first cycle, the statistical analysis revealed a 270 % increase in compressive force for the zinc-coated PCL stents (Figure S3 – Supplementary Information). Additionally, the compressive force of PLA-based stents increased by approximately 40 % and 20 % when applying Mg and Zn coatings, respectively.

When comparing the normalised values to those of commercially available stents, the results indicate that the produced stent yields similar outcomes for the same 25 % strain [139]. For example, Wei et al. [48] noted in their study that the commercially available stent (ABSORB™), made with PLA and featuring a 140 μm strut thickness, can withstand a force of around 0.2 N mm^{-1} at a 25 % strain. In this study, the force supported by the neat PLA-based structure is approximately 0.18 N mm^{-1}, increasing to around 0.25 N mm^{-1} when the stent is modified with coatings. It is worth noting that the produced stent has a lower thickness than the commercial stent, showcasing the efficiency of this new approach. On the other hand, PCL-based stents exhibit a lower value of normalised force, in line with the results of previous studies [140], even after surface modification.

Compressive strength values can also be expressed in pressure (kPa), calculated by considering the force exerted by the plate and the surface area of the stent in contact with the plates during the test [47]. In this study, the maximum pressure at 25 % of strain was compared to the average blood pressure of patients with atherosclerosis. Typically, average blood pressure has a mean value of 100 mmHg (12.5 kPa), fluctuating between a diastolic value of 80 mmHg and a systolic value of 120 mmHg [134]. According to the World Health Organization (WHO), individuals with clinical conditions such as atherosclerosis often have hypertension, which is when the pressure is too high, usually around 160/95 mmHg (21/12 kPa) with an average blood pressure of 117 mmHg (15 kPa) [141–143]. Fig. 26 displays the maximum pressure during the first cycle compared to the average blood pressure.

One of the objectives of this mechanical test was to assess the capacity of the stents to withstand the forces exerted by the artery wall. Given the complex loading circumstances *in vivo*, an extreme deformation of 25 % was applied as a safety measure to guarantee the capacity of the stents to endure substantial deformations without fractures. It was observed that the stents exhibited no visible fractures when subjected to a 25 % deformation during both the initial cycle and subsequent cycles.

However, based on the findings in the literature, it is evident that stents generally undergo deformations ranging from 3 % to 10 % during diastolic and systolic movements, depending on their design and material composition [6]. Considering the average blood pressure of a patient with hypertension, PLA-based stents exhibited an average strain of 11 %, 5 %, and 2 % for PLA, PLA + Mg, and PLA + Zn stents, respectively, while PCL stents showed an average strain of 11 %, 9 %, and 5 % for PCL, PCL + Mg, and PCL + Zn- stents, respectively. The results of this specific mechanical test indicate slight deformation within the elastic limit of the device for all material configurations. Consequently, there is no additional permanent deformation in coronary stents after placement and for a specific blood pressure within a damaged artery. Additionally, this behaviour prevents the displacement caused by the decrease in diameter due to the forces exerted by the artery. Therefore, concluding that the produced stents demonstrated promising outcomes is reasonable.

Fig. 27 shows the representative curves of the normalised force versus strain ratio during the different cycles for each material configuration. Upon analysing the representative curves of the normalised compressive force versus strain ratio during various cycles, it is evident that the first hysteresis loop does not fully close. The result indicates significant residual deformation resulting from cyclic loading and unloading within the specimens at 25 % of deformation. The hysteresis loops exhibit wide dispersion in the first cycle, but their distribution becomes increasingly concentrated with more cycles. Furthermore, the analysis of the maximum normalised force (Fig. 25) confirms a diminishing trend with an increase in the cycle number, especially notable in the case of the surface-modified PLA. Regardless, it is essential to mention that cyclic compression tests were conducted applying a 25 % deformation, an extreme *in vivo* condition. As previously mentioned, the strain experienced by the artery during movement is approximately 10 %.

Since a cyclic test was done, other parameters were considered for this study. One was the energy consumption per unit volume (S_h) calculated for each cycle. Also, the dynamic elastic modulus ($E_{dynamic}$) (Equation (10)) and the damping ratio (λ_R) (Equation (11)) were calculated for each cycle, considering the S_h and the area (A_S) of the triangle AOG (Fig. 28) [144,145]. Fig. 28 depicts a schematic hysteresis loop diagram for one cycle. The area under the loading curve (S_{re} – ABCEF) represents the energy per unit volume obtained from the load in the cycle, while the area under the unloading curve (S_{un} – ADCEF) represents the elastic deformation energy per unit volume released in one cycle. The difference between the two areas (S_h) corresponds to the energy consumption per unit volume in the cycle [144,145]. The hysteresis loop area was calculated by applying the integral method, with a second-order Savitzky-Golay smoothing performed with a threshold of 0.05. The OriginPro® 2018 software was used for this intention. Fig. 29 (also Figure S4 – Supplementary Information) and Fig. 30 display the results from the dynamic elastic modulus and damping ratio variation through the different cycles.

$$E_{dynamic} = \frac{\sigma_{dmax} - \sigma_{dmin}}{\varepsilon_{dmax} - \varepsilon_{dmin}} \qquad \text{Equation 10}$$

$$\lambda_R = \frac{S_h}{4\pi A_s} \qquad \text{Equation 11}$$

The literature suggests that a larger hysteresis ring area indicates increased energy loss, higher damping, and augmented plastic deformation [146]. It has been observed that cyclic stress at a 25 % strain ratio significantly impacts the mechanical properties of stents, possibly resulting in post-implantation displacement [6]. Initially, stents undergo notable plastic deformation, but this deformation stabilises after several cycles, as evidenced by reduced hysteresis loop area and stabilised compressive force values. This behaviour aligns with the viscoelastic/plastic nature of biodegradable polymers, which are known to absorb
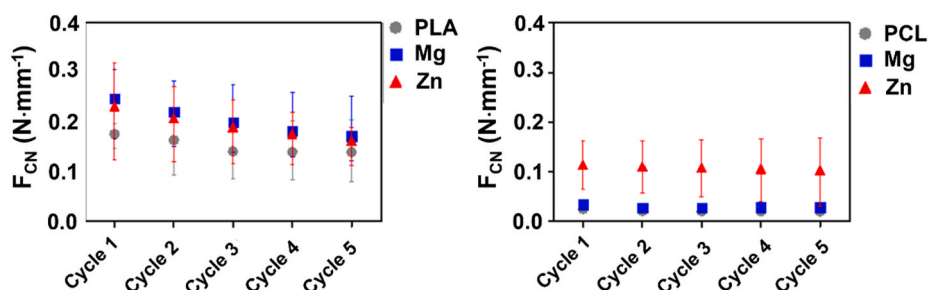

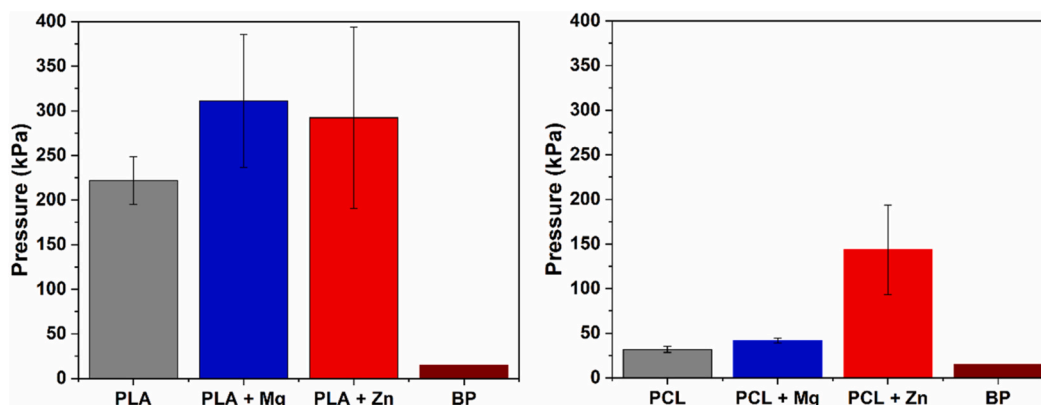**Fig. 25.** Values of the maximum compressive normalised force (mean ± SD) during the cyclic tests.

Fig. 26. Maximum pressure (mean ± SD) suffered by the stents during the first cycle (BP is the average blood pressure in a patient with hypertension).

and dissipate energy during dynamic loading. These findings agree with existing literature [147]. For example, Meng et al. [148] noted that pristine PCL exhibited higher initial hysteresis loops that decreased with subsequent cycles, particularly with increasing deformation strain.

Similarly, PLA-based stents displayed a higher hysteresis area in the first compression cycle [149]. Other parameters confirming this trend are the dynamic elastic modulus and damping ratio. Both parameters decline with increasing cycle numbers, indicating plastic deformation in the stent samples. The accumulation rate of plastic deformation diminishes over time, gradually decreasing the damping ratio and dynamic elastic modulus (Table S1 – Supplementary Information). As mentioned, the energy dissipation observed in this study can be attributed to viscoelastic dissipation, a notable mechanism in which internal friction and molecular rearrangements contribute to energy loss and plastic deformation [150].

Additionally, the maximum compressive force decreases with increasing cycles for all material configurations, indicating a decline in mechanical strength and lower modulus values over time. The reduction in hysteresis surface area with increasing cycles suggests that the stents attain a stable configuration, thereby reducing energy dissipation over time [6]. These observations reflect the overall behaviour throughout the tests, given that fatigue is an ongoing process [150]. In comparing pristine polymers with surface-modified ones, the surface-modified stents exhibit higher values of dynamic elastic modulus, indicating superior mechanical performance. Regarding the damping ratio, the values are relatively similar, attributed to the polymeric base structure of the stents [31]. At the time of writing this manuscript, the authors are unaware of any studies that assess how sputtered coatings influence cyclic compression in polymer-based stents. However, some researchers [6,31] have highlighted the effects of incorporating Mg and Zn microparticles into the PLA/PCL matrix, demonstrating that both configurations—polymeric stents with and without these particles—dissipate approximately the same amount of energy due to the polymeric substrate [6,31]. The prior information offers valuable context to explain the data provided in the present study.

Nevertheless, it is crucial to consider that the strain utilised in this study is significantly higher than *in vivo,* and the strain rate is much lower than the velocity of the diastolic and systolic movements.

Compared to the clinical gold standard (CoCr stents), polymer-based stents exhibit lower mechanical properties, such as compressive strength [134]. However, the compressive strength determined in this study appears sufficient to support arterial pressure, and the materials used are known for their compatibility and benefits *in vitro*, as previously demonstrated. The materials tested in this study demonstrated higher pressure resistance than those reported in earlier studies, indicating their potential for maintaining arterial pressure under cyclic loading conditions.

In future research, it is essential to incorporate cyclic compression of the stent at a lower deformation ratio with an increased strain rate to simulate the movements occurring in the artery. Additionally, conducting dynamic mechanical analysis (DMA) and performing differential scanning calorimetry (DSC) on the stents after cyclic compression is important to investigate any molecular rearrangements. These analyses will provide a more comprehensive understanding of the material behaviour of the stents and their potential long-term performance.

3.5.3. Crush resistance

This test aimed to determine the minimum load and deformation necessary to induce clinically significant compression, resulting in stent fracture, by reducing the stent diameter by at least 50 % [151]. Fig. 31 shows the compressive force vs. strain curves for uncoated and coated stents. Figs. 32 and 33 demonstrate the values of the maximum compressive force (crush resistance) and compressive modulus (E_C) as Mean ± SD.

This work compared the crush resistance of coated and uncoated stents by analysing their maximum compressive force and deformation percentage until fracture. The results indicated that the surface modification of the polymeric stents with a metallic coating significantly improved both the crush resistance and the compressive modulus of the medical devices, particularly evident in the case of PCL.

In the case of PLA-based samples, it was observed that the crush resistance is higher in the coated samples, with an increase of around 37 % and 34 % for magnesium and zinc coatings, respectively. The same trend was observed in the compressive modulus value, which increased by around 40 % for the coated samples compared to the uncoated ones, indicating higher stiffness or resistance to compression of the device. However, the untreated PLA and coated stents showed initiated fracture before reaching the pre-defined maximum strain. This behaviour is more noticeable in surface-engineered samples, where the fracture begins at an average deformation of almost 40 % (Figure S5 – Supplementary Information). The results are attributed to the higher compressive modulus value, which increases stiffness and makes the device more brittle and prone to fracture after a certain percentage of deformation [152].

From the literature survey, no studies were found that combined a bioresorbable polymeric structure with a biodegradable metallic coating. However, some studies have used PLA-based devices. For instance, Wei et al. [48] developed a new stent design made with PLA and compared it with the polymeric commercial stent ABSORB™. The authors found a maximum compressive force ranging between 0.08 N mm^{-1} and 0.1 N mm^{-1} for the commercially available stent and the new design, respectively. Another study by Thakur et al. [139] found similar values of maximum compressive force, with fracture occurring at a deformation percentage of around 20–30 %. In the present research, it was found that it is possible to increase the compressive force or crush resistance compared to what is found in the market, for instance, by only
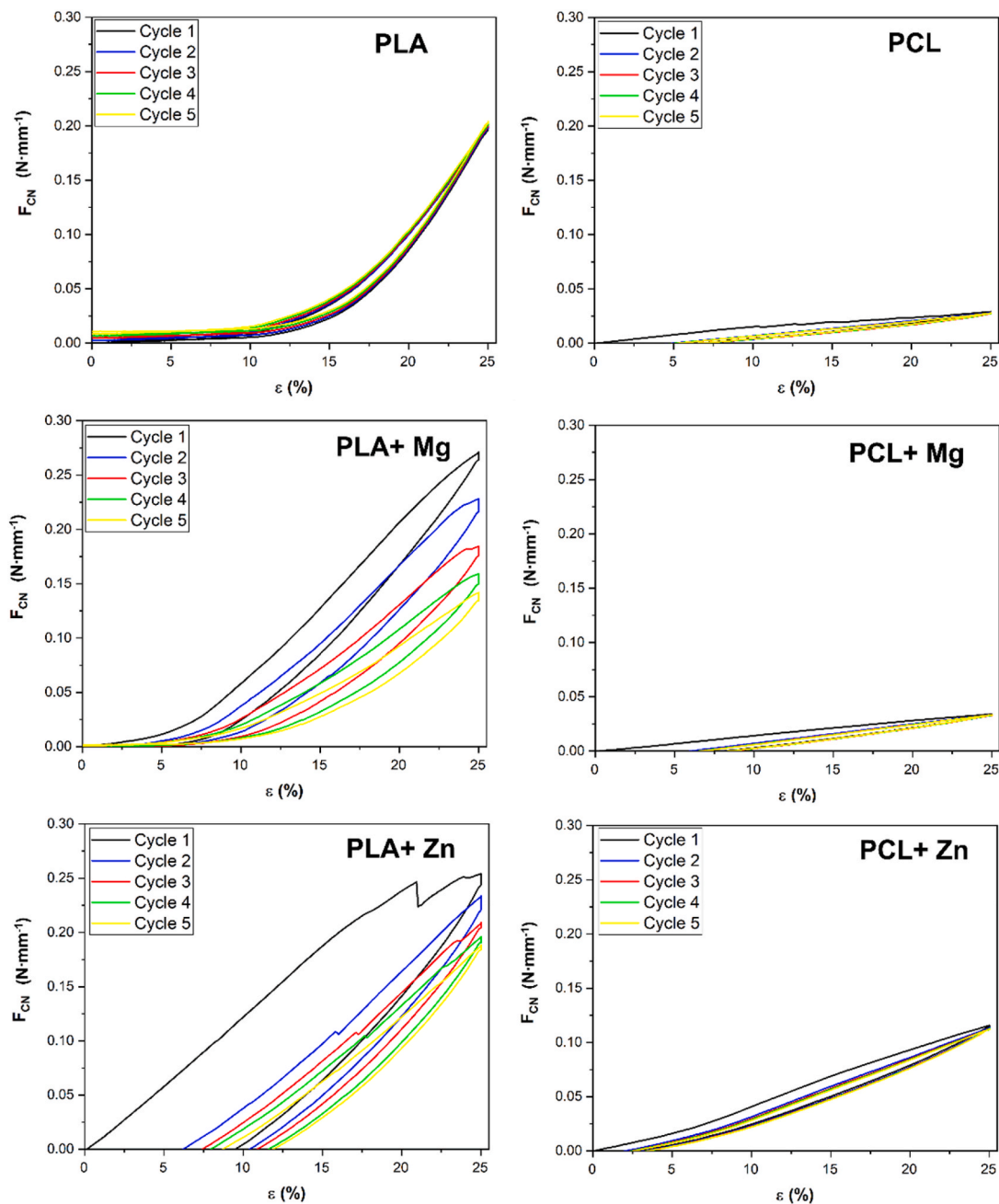
Fig. 27. Representative curves of the normalised compressive force vs. strain during the cyclic tests.

modifying the surface with a metallic coating [139]. Also, the percentage of deformation at which fracture begins is increased compared to the literature, establishing a safer limit for clinical practice.

Regarding PCL-based stents, there is a significant increase in compressive force when comparing pristine and coated polymers, especially in the case of zinc-coated samples. The compressive force in these samples rises by approximately 74 %, a statistically significant improvement over the neat material. Additionally, the compressive modulus shows a 61 % increase for Zn-coated samples. However, it is important to note that the Zn-coated samples exhibited signs of starting to fracture near the end of the test, a behaviour not observed in the case of neat PCL and Mg-coated samples. Although no studies have explicitly recommended using PCL coated with a biodegradable metallic coating for coronary stent applications, certain studies have provided insights into the behaviour of PCL-based stents during crush resistance tests. For example, the Han et al. [112] study demonstrated that an F_{CN} of 0.01 N

mm^{-1} is required to compress a PCL-based stent by 40 %. Another study by Zhao and colleagues [138] involved the creation of a new coronary stent by mixing PLA/PCL with two different compositions (95 %/5 % and 85 %/15 %), determining F_{CN} of 0.13 N mm^{-1} and 0.11 N mm^{-1}, respectively [138]. In the specific context of the discussed research, the F_{CN} of PCL was 0.06 N mm^{-1}, which increased to 0.08 N mm^{-1} and 0.23 N mm^{-1} for Mg-coated and Zn-coated stents, respectively. This suggests that combining PCL and Zn coating could enhance crush resistance compared to literature and commercial stents (0.08 N/mm – ABSORB™) and achieve a compressive deformation of almost 50 %, thereby establishing a safer threshold for clinical practice.

The sole study describing a similar approach with a permanent polymer and coating [30] revealed a F_{CN} of 0.11 N mm^{-1} for a permanent polymeric stent made with a photosensitive material (BMF Material Technology Inc.) modified with Au coating. As previously mentioned, the research approach of the present study is particularly innovative due
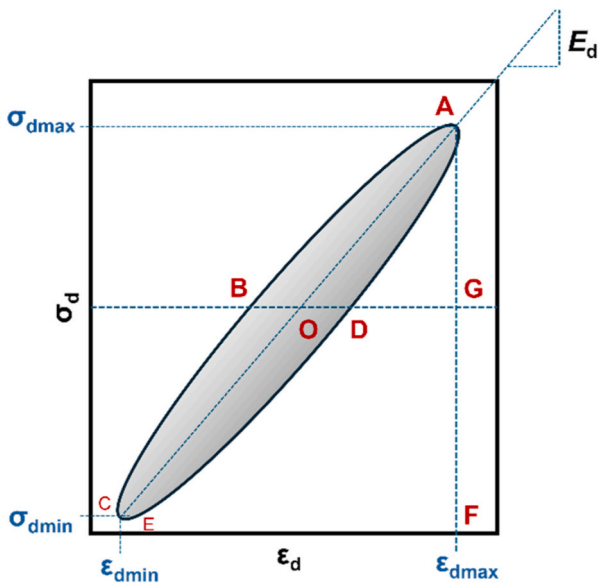
Fig. 28. Diagram of the hysteresis loop in the stress-strain curve (σ_{dmax} and σ_{dmin} are the maximum and minimum stress in a hysteresis loop.

to the biodegradability and safety of both materials involved in the human body.

Additionally, it has been observed that both coated PLA and PCL exhibit improved mechanical properties. Notably, in the case of zinc-coated PCL, it not only demonstrates superior crush resistance compared to the commercial stent and pure PLA but can withstand deformation without fracturing, unlike all the coated PLA samples. In summary, considering the crush resistance outcomes, PCL modified with zinc presents the most favourable combination of results regarding maximum compressive force and percentage of deformation, thus offering safer possibilities in clinical applications.

4. Conclusions

The primary goal of this study was to explore the impact of metallic coatings on the performance of polymeric-based stents. The initial part was focused on examining how coatings affected biological response and radiopacity, while the second part evaluated the mechanical properties of the surface-modified stents. The key conclusions are:

- Both metallic coatings improved antibacterial properties by inhibiting the growth of selected bacterial strains, particularly *S. aureus*, which is responsible for post-stenting bacterial infections. However, the degradation rate of Mg during the tests was excessively rapid, which could impact the healing process.
- Pristine polymers and Mg-coated ones exhibited higher thrombogenicity. In contrast, Zn-coated polymers displayed inherent anticoagulant properties without forming a thrombus during the test period.
- Concerning radiopacity, the zinc coating demonstrated excellent potential for enhancing contrast in medical images, making the stent visible during PCI, unlike Mg-coating or neat polymeric base structures.
- The presence of a coating reduced the yield strength, evaluated by tensile tests, indicating that for the same displacement, plastic deformation would increase while elastic recoil would decrease. The evaluation of electrical properties during the mechanical test also confirmed that the coatings remained adhered to the polymeric substrate, a critical factor in determining the performance of the surface-modified stent during expansion.
- The results of the cyclic compression indicate a significant improvement in the cyclic compressive force due to the coatings. Specifically, the zinc-coated PCL stents showed a 270 % increase, while PLA coated with Mg and Zn exhibited approximately 40 % and 20 % improvements, respectively. Furthermore, the cyclic compression tests highlighted a decrease in the dynamic elastic modulus over multiple cycles, with stabilisation observed after a certain number of cycles, particularly in PCL-coated stents.
- The study of the crush resistance revealed that the coated polymers demonstrated higher compressive force than the uncoated polymers.
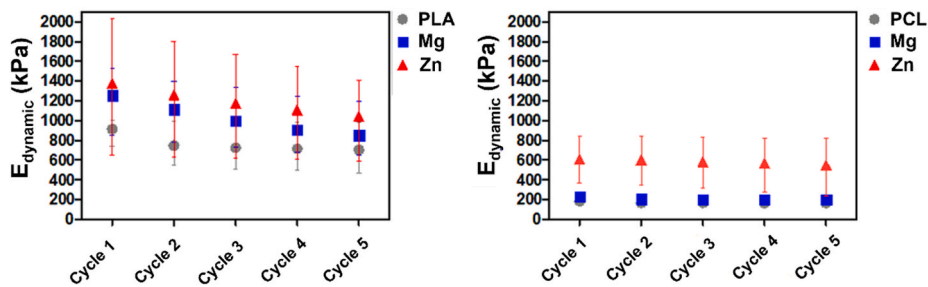

Fig. 29. Variation of the dynamic elastic modulus (mean ± SD) during the cyclic tests.
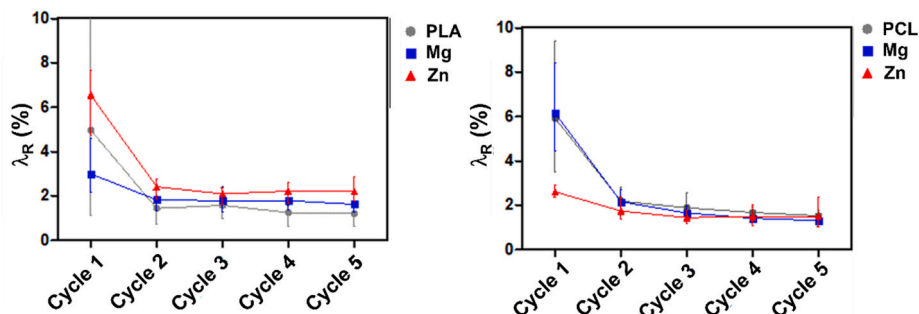

Fig. 30. Variation of the damping ratio (mean ± SD) during the cyclic tests.
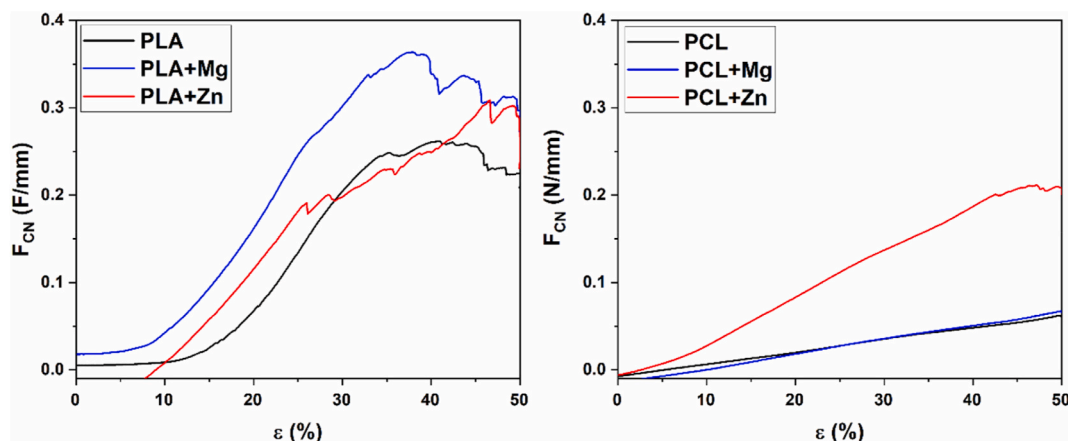
Fig. 31. Representative curves of crush resistance of the uncoated and coated stents: normalised compressive force vs. strain.
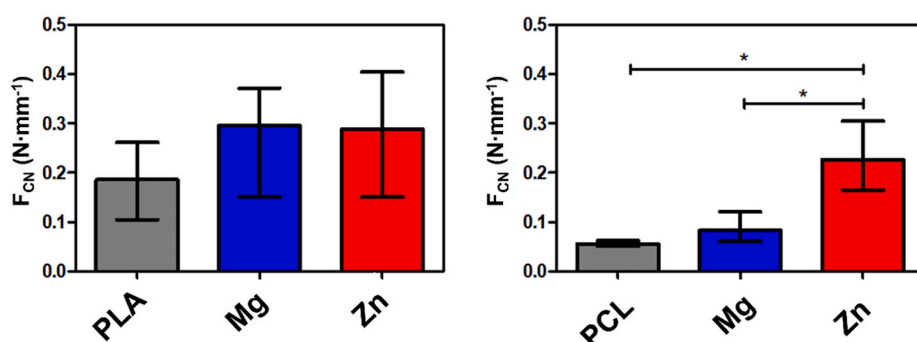

Fig. 32. Maximum compressive strength (crush resistance) (mean $\pm$ SD) for the coated and uncoated stents.
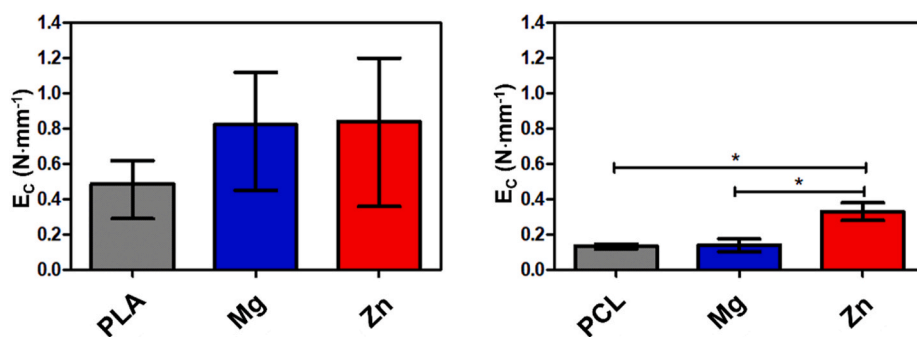

Fig. 33. Compressive modulus (mean $\pm$ SD) for the coated and uncoated stents.

It was observed that PLA-coated stents were more prone to fracture than the surface-modified PCL. However, both modified polymers displayed greater resistance to fracture compared to previous research. The findings indicate that combining Zn-coated PCL offers the best crush resistance performance.

The research findings indicate that the properties and characteristics of the polymeric stents were enhanced through the deposition of a sputtered zinc coating. Zinc, the second most abundant metal in the human body, does not initiate redox reactions under physiological conditions when in a free ion state. Additionally, samples coated with zinc inhibited the growth of microorganisms and exhibited inherent anticoagulant properties without the need for pharmaceutical incorporation, making them highly functional coatings. Zinc-modified stents provided improved mechanical strength to support the forces exerted by the artery wall, and the integrity of the film was maintained during

expansion. Finally, the zinc coating demonstrated excellent radiopacity, allowing the stent to be visible in medical images during the PCI.

To gain insight into future prospects, it is crucial to conduct tests using endothelial cells to explore the adhesion, growth, and proliferation on the modified surfaces and their cellular compatibility. Furthermore, additional mechanical tests are necessary, specifically those involving cyclic compression with a lower percentage of strain and a higher strain rate to emulate the biological environment. Likewise, *in vivo* tests must be conducted to validate the data obtained during this research.

CRediT authorship contribution statement

Ana M. Sousa: Writing – original draft, Visualization, Methodology, Investigation, Formal analysis. **Rita Branco:** Writing – review & editing, Methodology, Investigation. **Paula V. Morais:** Writing – review &

editing, Resources. **Manuel F. Pereira:** Writing – review & editing, Resources, Methodology, Investigation. **Ana M. Amaro:** Writing – review & editing, Supervision, Formal analysis. **Ana P. Piedade:** Writing – review & editing, Supervision, Project administration, Funding acquisition, Conceptualization.

Ethics approval and consent to participate

Human volunteers provided the whole blood used in this study. All procedures followed the ethical standards of the institutional and/or national research committee and with the 1964 Helsinki Declaration and its later amendments or comparable ethical standards. Informed consent: Informed consent was obtained from the participant included in the study.

Declaration of generative AI and AI-assisted technologies in the writing process

During the preparation and writing of this work, the authors did not use generative AI or AI-assisted technologies.

Funding

Declaration of competing interest

The authors declare that they have no known competing financial interests or personal relationships that could have appeared to influence the work reported in this paper.

Acknowledgements

Appendix A. Supplementary data

Supplementary data to this article can be found online at https://doi.org/10.1016/j.bioactmat.2024.12.003.

References

[1] L. Wang, R. Xu, L. Meng, Q. Zhang, Z. Qian, J. Chen, C. Pan, A fucoidan-loaded hydrogel coating for enhancing corrosion resistance, hemocompatibility and endothelial cell growth of magnesium alloy for cardiovascular stents, Biomater. Adv. 163 (2024) 213960, https://doi.org/10.1016/j.bioadv.2024.213960.

[2] A.M. Sousa, A.M. Amaro, A.P. Piedade, Structural design optimization through finite element analysis of additive manufactured bioresorbable polymeric stents, Mater. Today Chem. 36 (2024) 101972, https://doi.org/10.1016/j.mtchem.2024.101972.

[3] A.M. Sousa, A.M. Amaro, A.P. Piedade, 3D printing of polymeric bioresorbable stents: a strategy to improve both cellular compatibility and mechanical properties, Polymers 14 (2022) 1099, https://doi.org/10.3390/polym14061099.

[4] S. McMahon, N. Bertollo, E.D.O. Cearbhaill, J. Salber, L. Pierucci, P. Duffy, T. Dürig, V. Bi, W. Wang, Bio-resorbable polymer stents: a review of material progress and prospects, Prog. Polym. Sci. 83 (2018) 79–96, https://doi.org/10.1016/j.progpolymsci.2018.05.002.

[5] N. Bink, V.B. Mohan, S. Fakirov, Recent advances in plastic stents: a comprehensive review, Int. J. Polym. Mater. Polym. Biomater. (2021), https://doi.org/10.1080/00914037.2019.1685519.

[6] A. Srivastava, N. Kumari, M. Agarwal, P. Bhati, N. Bhatnagar, Fabrication and characterization of bioresorbable radiopaque PLLA/PCL/Mg alloy composite tubes for cardiovascular stent application, Int. J. Polym. Mater. Polym. Biomater. 73 (2024) 564–580, https://doi.org/10.1080/00914037.2023.2182783.

[7] K.-H. Cheon, C. Park, M.-H. Kang, S. Park, J. Kim, S.-H. Jeong, H.-E. Kim, H.-D. Jung, T.-S. Jang, A combination strategy of functionalized polymer coating with Ta ion implantation for multifunctional and biodegradable vascular stents,
J. Magnesium Alloys 9 (2021) 2194–2206, https://doi.org/10.1016/j.jma.2021.07.019.

[8] C.K. Emonde, M.-E. Eggers, M. Wichmann, C. Hurschler, M. Ettinger, B. Denkena, Radiopacity enhancements in polymeric implant biomaterials: a comprehensive literature review, ACS Biomater. Sci. Eng. 10 (2024) 1323–1334, https://doi.org/10.1021/acsbiomaterials.3c01667.

[9] C. Park, S. Park, J. Kim, A. Han, S. Ahn, S.-K. Min, H.J. Jae, J.W. Chung, J.-H. Lee, H.-D. Jung, H.-E. Kim, T.-S. Jang, Enhanced endothelial cell activity induced by incorporation of nano-thick tantalum layer in artificial vascular grafts, Appl. Surf. Sci. 508 (2020) 144801, https://doi.org/10.1016/j.apsusc.2019.144801.

[10] J. Dong, M. Pacella, Y. Liu, L. Zhao, Surface engineering and the application of laser-based processes to stents - a review of the latest development, Bioact. Mater. 10 (2022) 159–184, https://doi.org/10.1016/j.bioactmat.2021.08.023.

[11] S.L. Nica, C. Hulubei, D. Popovici, M. Dobromir, Metallized polyimide films for biomedical applications: X-ray photoelectron spectroscopy, surface tension, and blood compatibility studies, Polym. Eng. Sci. 62 (2022) 648–663, https://doi.org/10.1002/pen.25872.

[12] S. Sharma, V. Gupta, D. Mudgal, Current trends, applications, and challenges of coatings on additive manufacturing based biopolymers: a state of art review, Polym. Compos. 43 (2022) 6749–6781, https://doi.org/10.1002/pc.26809.

[13] T. Govindarajan, R. Shandas, A survey of surface modification techniques for next-generation shape memory polymer stent devices, Polymers 6 (2014) 2309–2331, https://doi.org/10.3390/polym6092309.

[14] R. Melentiev, A. Yudhanto, R. Tao, T. Vuchkov, G. Lubineau, Metallization of polymers and composites: state-of-the-art approaches, Mater. Des. 221 (2022) 110958, https://doi.org/10.1016/j.matdes.2022.110958.

[15] R.A. Pareta, A.B. Reising, T. Miller, D. Storey, T.J. Webster, Increased endothelial cell adhesion on plasma modified nanostructured polymeric and metallic surfaces for vascular stent applications, Biotechnol. Bioeng. 103 (2009) 459–471, https://doi.org/10.1002/bit.22276.

[16] A.S. Raikar, S. Priya, S.P. Bhilegaonkar, S.N. Somnache, D.M. Kalaskar, Surface engineering of bioactive coatings for improved stent hemocompatibility: a comprehensive review, Materials 16 (2023), https://doi.org/10.3390/ma16216940.

[17] D.J. da Silva, G.S. Ferreira, A. Duran, F.L.A. Fonseca, D.F. Parra, R.F. Bueno, D.S. Rosa, Copper coatings on poly(lactic acid) via rapid magnetron sputtering: morphology, chemistry, and antimicrobial performance against bacteria and SARS-CoV-2, Mater, Today Commun. 34 (2023) 105440, https://doi.org/10.1016/j.mtcomm.2023.105440.

[18] E. Mostaed, M. Sikora-Jasinska, J.W. Drelich, M. Vedani, Zinc-based alloys for degradable vascular stent applications, Acta Biomater. 71 (2018) 1–23, https://doi.org/10.1016/j.actbio.2018.03.005.

[19] C. Pan, C. Zuo, J. Chen, Q. Zhang, L. Deng, Y. Liu, P. Ding, Constructing sodium alginate/carboxymethyl chitosan coating capable of catalytically releasing NO or CO for improving the hemocompatibility and endothelialization of magnesium alloys, Int. J. Biol. Macromol. 279 (2024) 135166, https://doi.org/10.1016/j.ijbiomac.2024.135166.

[20] S.A. Sreenivasamurthy, F.F. Akhter, A. Akhter, Y. Su, D. Zhu, Cellular mechanisms of biodegradable zinc and magnesium materials on promoting angiogenesis, Biomater. Adv. 139 (2022) 213023, https://doi.org/10.1016/j.bioadv.2022.213023.

[21] S. Prasadh, S. Raguraman, R. Wong, M. Gupta, Current status and outlook of temporary implants (Magnesium/Zinc) in cardiovascular applications, Metals 12 (2022), https://doi.org/10.3390/met12060999.

[22] N. Beshchasna, M. Saqib, H. Kraskiewicz, Ł. Wasyluk, O. Kuzmin, O.C. Duta, D. Ficai, Z. Ghizdavet, A. Marin, A. Ficai, Z. Sun, V.F. Pichugin, J. Opitz, E. Andronescu, Recent advances in manufacturing innovative stents, Pharmaceutics 12 (2020) 349, https://doi.org/10.3390/pharmaceutics12040349.

[23] J. Fu, Y. Su, Y.-X. Qin, Y. Zheng, Y. Wang, D. Zhu, Evolution of metallic cardiovascular stent materials: a comparative study among stainless steel, magnesium and zinc, Biomaterials 230 (2020) 119641, https://doi.org/10.1016/j.biomaterials.2019.119641.

[24] F. El-Taib Heakal, A.M. Bakry, Serum albumin can influence magnesium alloy degradation in simulated blood plasma for cardiovascular stenting, Mater. Chem. Phys. 220 (2018) 35–49, https://doi.org/10.1016/j.matchemphys.2018.08.060.

[25] P. Li, J. Dai, Y. Li, D. Alexander, J. Čapek, J. Geis-Gerstorfer, G. Wan, J. Han, Z. Yu, A. Li, Zinc based biodegradable metals for bone repair and regeneration: bioactivity and molecular mechanisms, Mater. Today Bio. 25 (2024) 100932, https://doi.org/10.1016/j.mtbio.2023.100932.

[26] E. Kozlova, E. Sherstyukova, V. Sergunova, A. Kozlov, O. Gudkova, V. Inozemtsev, A. Chernysh, The toxic influence of excess free iron on red blood cells in the biophysical experiment: an in vitro study, J. Toxicol. 2022 (2022) 1–16, https://doi.org/10.1155/2022/7113958.

[27] S. Chamnongpol, W. Dodson, M.J. Cromie, Z.L. Harris, E.A. Groisman, Fe(III)-mediated cellular toxicity, Mol. Microbiol. 45 (2002) 711–719, https://doi.org/10.1046/j.1365-2958.2002.03041.x.

[28] A.P. Piedade, F. Romeu, R. Branco, P.V. Morais, 8 - thin films for medical and environmental applications, in: L. Nánai, A. Samantara, L. Fábián, S. Ratha (Eds.), Methods Film Synth. Coat. Proced., IntechOpen, London, 2020, pp. 107–121, https://doi.org/10.5772/intechopen.80021.

[29] X. Liu, D.M. Grant, A.J. Parsons, L.T. Harper, C.D. Rudd, I. Ahmed, Magnesium coated bioresorbable phosphate glass fibres: investigation of the interface between fibre and polyester matrices, BioMed Res. Int. 2013 (2013) 735981, https://doi.org/10.1155/2013/735981.

[30] R. Xiao, X. Feng, W. Liu, W. Zhou, X. Li, I. Song, M. Ding, Y. Pu, D. Zhang, R. Fan, T.-H. Chen, Y. Lu, Direct 3D printing of thin-walled cardiovascular stents with negative Poisson's ratio (NPR) structure and functional metallic coating, Compos. Struct. 306 (2023) 116572, https://doi.org/10.1016/j.compstruct.2022.116572.

[31] A. Srivastava, S. Singh, M. Agrawal, P. Bhati, N. Kumari, M. Pandya, P. Vashisth, P. Chauhan, N. Bhatnagar, Fabrication and characterization of PLLA/PCL/Mg-Zn-Y alloy composite stent, Polym. Eng. Sci. 64 (2024) 243–253, https://doi.org/10.1002/pen.26543.

[32] F. El-Taib Heakal, A.M. Bakry, Serum albumin can influence magnesium alloy degradation in simulated blood plasma for cardiovascular stenting, Mater. Chem. Phys. 220 (2018) 35–49, https://doi.org/10.1016/j.matchemphys.2018.08.060.

[33] H. Habazaki, Corrosion of amorphous and nanograined alloys, in: Shreir's Corros., Elsevier, 2010, pp. 2192–2204, https://doi.org/10.1016/B978-044452787-5.00107-4.

[34] B. Abdallah, W. Zetoun, A. Tello, Deposition of ZnO thin films with different powers using RF magnetron sputtering method: structural, electrical and optical study, Heliyon 10 (2024) e27606, https://doi.org/10.1016/j.heliyon.2024.e27606.

[35] P. Malinský, P. Slepička, V. Hnatowicz, V. Švorčík, Early stages of growth of gold layers sputter deposited on glass and silicon substrates, Nanoscale Res. Lett. 7 (2012) 241, https://doi.org/10.1186/1556-276X-7-241.

[36] V.A. Pereira, P.V. Mendonça, R. Branco, P.V. Morais, J.F.J. Coelho, A.C. Serra, Bioactive surfaces with well-defined amphiphilic copolymers containing a natural terpene-based monomer, Prog. Org. Coating 183 (2023) 107791, https://doi.org/10.1016/j.porgcoat.2023.107791.

[37] A.P. Piedade, A.C. Pinho, R. Branco, P. V Morais, Evaluation of antimicrobial activity of ZnO based nanocomposites for the coating of non-critical equipment in medical-care facilities, Appl. Surf. Sci. 513 (2020) 145818, https://doi.org/10.1016/j.apsusc.2020.145818.

[38] V. Ramakumar, A. Thakur, R.S. Abdulkader, B. Claessen, A. Anandaram, R. Palraj, V.M. Aravamudan, M. Thoddi Ramamurthy, G. Dangas, N.B. Senguttuvan, Coronary stent infections — a systematic review and meta-analysis, Cardiovasc. Revascularization Med. 54 (2023) 16–24, https://doi.org/10.1016/j.carrev.2023.02.021.

[39] A.A. Singh, S. Sharma, M. Srivastava, A. Majumdar, Modulating the properties of polylactic acid for packaging applications using biobased plasticizers and naturally obtained fillers, Int. J. Biol. Macromol. 153 (2020) 1165–1175, https://doi.org/10.1016/j.ijbiomac.2019.10.246.

[40] A.F. Kanaan, A.P. Piedade, H.C. de Sousa, A.M.A. Dias, Semi-interpenetrating chitosan/ionic liquid polymer networks as electro-responsive biomaterials for potential wound dressings and iontophoretic applications, Mater. Sci. Eng. C 121 (2021) 111798, https://doi.org/10.1016/j.msec.2020.111798.

[41] M.S. Ibne Mahbub, T. Sultana, J.-G. Gwon, B.-T. Lee, Fabrication of thrombin loaded TEMPO-oxidized cellulose nanofiber-gelatin sponges and their hemostatic behavior in rat liver hemorrhage model, J. Biomater. Sci. Polym. Ed. 33 (2022) 499–516, https://doi.org/10.1080/09205063.2021.1992877.

[42] Council for International Organizations of Medical Sciences (CIOMS), World Health Organization (WHO), Declaration of Helsinki - ethical principles for medical research involving human subjects. https://www.who.int/docs/default-source/ethics/web-cioms-ethicalguidelines.pdf?sfvrsn=f62ee074_0, 2016. (Accessed 30 July 2024).

[43] ASTM International, ASTM F640-20, standard test methods for determining radiopacity for medical use, west conshohocken. https://doi.org/10.1520/F0640-20, 2023.

[44] J. Parracha, M. Pereira, A. Maurício, P. Faria, D.F. Lima, M. Tenório, L. Nunes, Assessment of the density loss in anobiid infested pine using X-ray micro-computed tomography, Buildings 11 (2021) 173, https://doi.org/10.3390/buildings11040173.

[45] R. Travincas, M.F.C. Pereira, I. Torres, A. Maurício, D. Silveira, I. Flores-Colen, X-ray microtomography applied to mortars: review of microstructural visualization and parameterization, Micron 164 (2023) 103375, https://doi.org/10.1016/j.micron.2022.103375.

[46] R. Baptista, M.F.C. Pereira, A. Maurício, D. Rechena, V. Infante, M. Guedes, Experimental and numerical characterization of 3D-printed scaffolds under monotonic compression with the aid of micro-CT volume reconstruction, Bio-Des. Manuf. 4 (2021) 222–242, https://doi.org/10.1007/s42242-020-00122-3.

[47] ISO - International Organization for Standardization, ISO 25539-2:2020 - cardiovascular implants — Endovascular devices, Part 2: vascular stents. https://www.iso.org/standard/69835.html, 2020. (Accessed 30 July 2024).

[48] Y. Wei, M. Wang, D. Zhao, H. Li, Y. Jin, Structural design of mechanical property for biodegradable polymeric stent, Adv. Mater. Sci. Eng. 2019 (2019) 2960435, https://doi.org/10.1155/2019/2960435.

[49] D. Jain, S. Pareek, A. Agarwala, R. Shrivastava, W. Sassi, S.K. Parida, D. Behera, Effect of exposure time on corrosion behavior of zinc-alloy in simulated body fluid solution: electrochemical and surface investigation, J. Mater. Res. Technol. 10 (2021) 738–751, https://doi.org/10.1016/j.jmrt.2020.12.050.

[50] M.M. Alves, T. Prošek, C.F. Santos, M.F. Montemor, Evolution of the in vitro degradation of Zn–Mg alloys under simulated physiological conditions, RSC Adv. 7 (2017) 28224–28233, https://doi.org/10.1039/C6RA28542B.

[51] E. Pakhomova, A. Varone, A. Mezzi, A. Fava, C. Manis, F. Loy, A. Palombi, G. Cao, Surface characterization of AZ31 alloy after long-term immersion in simulated body fluid, Crystals 13 (2023) 1692, https://doi.org/10.3390/cryst13121692.

[52] D. Vaz, A.P. Piedade, Structure and mechanical properties of a copper combustion chamber throughout its life cycle, Metals 8 (2018) 362, https://doi.org/10.3390/met8050362.

[53] H.Y. Ang, H. Bulluck, P. Wong, S.S. Venkatraman, Y. Huang, N. Foin, Bioresorbable stents: current and upcoming bioresorbable technologies, Int. J. Cardiol. 228 (2017) 931–939, https://doi.org/10.1016/j.ijcard.2016.11.258.

[54] A.A. Ermina, N.S. Solodovchenko, K. V Prigoda, V.S. Levitskii, V.O. Bolshakov, M. Yu Maximov, Y.M. Koshtyal, S.I. Pavlov, V.A. Tolmachev, Y.A. Zharova, Silver particles embedded in silicon: the fabrication process and their application in surface enhanced Raman scattering (SERS), Appl. Surf. Sci. 608 (2023) 155146, https://doi.org/10.1016/j.apsusc.2022.155146.

[55] M.M. Alves, T. Prošek, C.F. Santos, M.F. Montemor, Evolution of the in vitro degradation of Zn–Mg alloys under simulated physiological conditions, RSC Adv. 7 (2017) 28224–28233, https://doi.org/10.1039/C6RA28542B.

[56] C. Larre, Y. Morizet, C. Guillot-Deudon, F. Baron, N. Mangold, Quantitative Raman calibration of sulfate-bearing polymineralic mixtures: a S quantification in sedimentary rocks on Mars, Mineral. Mag. 83 (2019) 57–69, https://doi.org/10.1180/mgm.2018.147.

[57] G.-L. Song, 1 - corrosion electrochemistry of magnesium (Mg) and its alloys, in: G. B.T. C, M.A. Song (Eds.), Woodhead Publ. Ser. Met. Surf. Eng., Woodhead Publishing, 2011, pp. 3–65, https://doi.org/10.1533/9780857091413.1.3.

[58] M. Dekermenjian, A.P. Ruediger, A. Merlen, Raman spectroscopy investigation of magnesium oxide nanoparticles, RSC Adv. 13 (2023) 26683–26689, https://doi.org/10.1039/d3ra04492k.

[59] S. Shafyra, E.M. Nazim, N.H. Ngadiman, I. Sudin, Comparative study on the microstructure and biodegradation behavior of commercialized pure Mg and Mg-1.0Ca-0.5Sr alloy in 27 mM HCO3−-SBF: the influence of the pH regulation treatments, Metals 13 (2023) 136, https://doi.org/10.3390/met13010136.

[60] J. Gonzalez, R.Q. Hou, E.P.S. Nidadavolu, R. Willumeit-Römer, F. Feyerabend, Magnesium degradation under physiological conditions – best practice, Bioact. Mater. 3 (2018) 174–185, https://doi.org/10.1016/j.bioactmat.2018.01.003.

[61] B. Lafuente, R.T. Downs, H. Yang, N. Stone, The power of databases: the RRUFF project, in: T. Armbruster, R.M. Danisi (Eds.), Highlights Mineral. Crystallogr., W. De Gruyter, Berlin, Germany, 2015, pp. 1–30. https://rruff.info/.

[62] M. Silambarasan, S. Saravanan, T. Soga, Raman and photoluminescence studies of Ag and Fe-doped ZnO nanoparticles, Int. J. ChemTech Res. (2015) 1644–1650. https://api.semanticscholar.org/CorpusID:220513610.

[63] V.I. Korepanov, S.-Y. Chan, H.-C. Hsu, H. Hamaguchi, Phonon confinement and size effect in Raman spectra of ZnO nanoparticles, Heliyon 5 (2019) e01222, https://doi.org/10.1016/j.heliyon.2019.e01222.

[64] X. Liu, H. Yang, Y. Liu, P. Xiong, H. Guo, H.-H. Huang, Y. Zheng, Comparative studies on degradation behavior of pure zinc in various simulated body fluids, JOM (J. Occup. Med.) 71 (2019) 1414–1425, https://doi.org/10.1007/s11837-019-03357-3.

[65] C. García-Mintegui, L.C. Córdoba, J. Buxadera-Palomero, A. Marquina, E. Jiménez-Piqué, M.-P. Ginebra, J.L. Cortina, M. Pegueroles, Zn-Mg and Zn-Cu alloys for stenting applications: from nanoscale mechanical characterization to in vitro degradation and biocompatibility, Bioact. Mater. 6 (2021) 4430–4446, https://doi.org/10.1016/j.bioactmat.2021.04.015.

[66] L. Liu, Y. Meng, C. Dong, Y. Yan, A.A. Volinsky, L.-N. Wang, Initial formation of corrosion products on pure zinc in simulated body fluid, J. Mater. Sci. Technol. 34 (2018) 2271–2282, https://doi.org/10.1016/j.jmst.2018.05.005.

[67] X. Zhu, P. Guo, L. Yang, C. Xu, F. Geng, J. Shen, T. Lu, W. Sun, Z. Song, Comparison of the in vitro corrosion behavior of biodegradable pure Zn in SBF, 0.9% NaCl, and DMEM, Mater. Corros. 72 (2021) 1687–1701, https://doi.org/10.1002/maco.202112485.

[68] A.T. Al-Hinai, M.H. Al-Hinai, J. Dutta, Application of Eh-pH diagram for room temperature precipitation of zinc stannate microcubes in an aqueous media, Mater. Res. Bull. 49 (2014) 645–650, https://doi.org/10.1016/j.materresbull.2013.10.011.

[69] R. Chen, C. Zou, X. Yan, A. Alyamani, W. Gao, Growth mechanism of ZnO nanostructures in wet-oxidation process, Thin Solid Films 519 (2011) 1837–1844, https://doi.org/10.1016/j.tsf.2010.10.012.

[70] D. Jain, S. Pareek, A. Agarwala, R. Shrivastava, W. Sassi, S.K. Parida, D. Behera, Effect of exposure time on corrosion behavior of zinc-alloy in simulated body fluid solution: electrochemical and surface investigation, J. Mater. Res. Technol. 10 (2021) 738–751, https://doi.org/10.1016/j.jmrt.2020.12.050.

[71] S. Chen, T. Du, H. Zhang, J. Qi, Y. Zhang, Y. Mu, A. Qiao, Methods for improving the properties of zinc for the application of biodegradable vascular stents, Biomater. Adv. 156 (2024) 213693, https://doi.org/10.1016/j.bioadv.2023.213693.

[72] J. Cheng, B. Liu, Y.H. Wu, Y.F. Zheng, Comparative in vitro study on pure metals (Fe, Mn, Mg, Zn and W) as biodegradable metals, J. Mater. Sci. Technol. 29 (2013) 619–627, https://doi.org/10.1016/j.jmst.2013.03.019.

[73] R. Baboian, NACE Corrosion Engineer's Reference Guide, fourth ed., Nace International, 2016.

[74] E. Mostaed, M. Sikora-Jasinska, J.W. Drelich, M. Vedani, Zinc-based alloys for degradable vascular stent applications, Acta Biomater. 71 (2018) 1–23, https://doi.org/10.1016/j.actbio.2018.03.005.

[75] F. Azizian, H. Naffakh-Moosavy, F. Bagheri, The role of Cu addition in the metallurgical features, mechanical properties, and cytocompatibility of cardiovascular stents biodegradable Zn-based alloy, Intermetallics 164 (2024) 108106, https://doi.org/10.1016/j.intermet.2023.108106.

[76] A.A. Oliver, M. Sikora-Jasinska, A.G. Demir, R.J. Guillory, Recent advances and directions in the development of bioresorbable metallic cardiovascular stents: insights from recent human and in vivo studies, Acta Biomater. 127 (2021) 1–23, https://doi.org/10.1016/j.actbio.2021.03.058.

[77] X. Chen, R. Chang, H. Liu, L. Zhang, Y. Zheng, Moving research direction in the field of metallic bioresorbable stents-A mini-review, Bioact. Mater. 24 (2023) 20–25, https://doi.org/10.1016/j.bioactmat.2022.12.004.

[78] P. Li, J. Dai, Y. Li, D. Alexander, J. Čapek, J. Geis-Gerstorfer, G. Wan, J. Han, Z. Yu, A. Li, Zinc based biodegradable metals for bone repair and regeneration: bioactivity and molecular mechanisms, Mater. Today Bio. 25 (2024) 100932, https://doi.org/10.1016/j.mtbio.2023.100932.

[79] Z. Lin, X. Sun, H. Yang, The role of antibacterial metallic elements in simultaneously improving the corrosion resistance and antibacterial activity of magnesium alloys, Mater. Des. 198 (2021) 109350, https://doi.org/10.1016/j.matdes.2020.109350.

[80] S. Souaf Khalafi, G.A. Valencia Páez, A.L. Fernández González, Coronary stent infection: an unusual complication after percutaneous coronary intervention, port, J. Card. Thorac. Vasc. Surg. 30 (2023) 71–75, https://doi.org/10.48729/pjctvs.372.

[81] E. Pazos-Ortiz, J.H. Roque-Ruiz, E.A. Hinojos-Márquez, J. López-Esparza, A. Donohué-Cornejo, J.C. Cuevas-González, L.F. Espinosa-Cristóbal, S.Y. Reyes-López, Dose-dependent antimicrobial activity of silver nanoparticles on polycaprolactone fibers against gram-positive and gram-negative bacteria, J. Nanomater. 2017 (2017) 4752314, https://doi.org/10.1155/2017/4752314.

[82] L. Shao, Y. Xi, Y. Weng, Recent advances in PLA-based antibacterial food packaging and its applications, Molecules 27 (2022) 5953, https://doi.org/10.3390/molecules27185953.

[83] H. Lee, D.Y. Shin, Y. Na, G. Han, J. Kim, N. Kim, S.-J. Bang, H.S. Kang, S. Oh, C.-B. Yoon, J. Park, H.-E. Kim, H.-D. Jung, M.-H. Kang, Antibacterial PLA/Mg composite with enhanced mechanical and biological performance for biodegradable orthopedic implants, Biomater. Adv. 152 (2023) 213523, https://doi.org/10.1016/j.bioadv.2023.213523.

[84] Z. Mrozińska, M.B. Ponczek, A. Kaczmarek, M. Świerczyńska, M.H. Kudzin, Activity in the field of blood coagulation processes of poly(lactide)-zinc fiber composite material obtained by magnetron sputtering, Coatings 14 (2024) 666, https://doi.org/10.3390/coatings14060666.

[85] J. Tian, T.E. Paterson, J. Zhang, Y. Li, H. Ouyang, I.O. Asencio, P. V Hatton, Y. Zhao, Z. Li, Enhanced antibacterial ability of electrospun PCL scaffolds incorporating ZnO nanowires, Int. J. Mol. Sci. 24 (2023) 14420, https://doi.org/10.3390/ijms241914420.

[86] D.A. Robinson, R.W. Griffith, D. Shechtman, R.B. Evans, M.G. Conzemius, In vitro antibacterial properties of magnesium metal against Escherichia coli, Pseudomonas aeruginosa and Staphylococcus aureus, Acta Biomater. 6 (2010) 1869–1877, https://doi.org/10.1016/j.actbio.2009.10.007.

[87] H. Mohd Yusof, R. Mohamad, U.H. Zaidan, N.A. Abdul Rahman, Microbial synthesis of zinc oxide nanoparticles and their potential application as an antimicrobial agent and a feed supplement in animal industry: a review, J. Anim. Sci. Biotechnol. 10 (2019) 57, https://doi.org/10.1186/s40104-019-0368-z.

[88] Y. Xie, L. Yang, Calcium and magnesium ions are membrane-active against stationary-phase Staphylococcus aureus with high specificity, Sci. Rep. 6 (2016) 20628, https://doi.org/10.1038/srep20628.

[89] H. Feng, G. Wang, W. Jin, X. Zhang, Y. Huang, A. Gao, H. Wu, G. Wu, P.K. Chu, Systematic study of inherent antibacterial properties of magnesium-based biomaterials, ACS Appl. Mater. Interfaces 8 (2016) 9662–9673, https://doi.org/10.1021/acsami.6b02241.

[90] Z. Cui, F. Ge, Y. Lin, L. Wang, L. Lei, H. Tian, M. Yu, X. Wang, Corrosion behavior of AZ31 magnesium alloy in the chloride solution containing ammonium nitrate, Electrochim. Acta 278 (2018) 421–437, https://doi.org/10.1016/j.electacta.2018.05.059.

[91] P. Bhattacharya, A. Dey, S. Neogi, An insight into the mechanism of antibacterial activity by magnesium oxide nanoparticles, J. Mater. Chem. B 9 (2021) 5329–5339, https://doi.org/10.1039/D1TB00875G.

[92] N.-Y.T. Nguyen, N. Grelling, C.L. Wetteland, R. Rosario, H. Liu, Antimicrobial activities and mechanisms of magnesium oxide nanoparticles (nMgO) against pathogenic bacteria, yeasts, and biofilms, Sci. Rep. 8 (2018) 16260, https://doi.org/10.1038/s41598-018-34567-5.

[93] C.R. Mendes, G. Dilarri, C.F. Forsan, V. de M.R. Sapata, P.R.M. Lopes, P.B. de Moraes, R.N. Montagnolli, H. Ferreira, E.D. Bidoia, Antibacterial action and target mechanisms of zinc oxide nanoparticles against bacterial pathogens, Sci. Rep. 12 (2022) 2658, https://doi.org/10.1038/s41598-022-06657-y.

[94] C.A. Labarrere, A.E. Dabiri, G.S. Kassab, Thrombogenic and inflammatory reactions to biomaterials in medical devices, Front. Bioeng. Biotechnol. 8 (2020) 123, https://doi.org/10.3389/fbioe.2020.00123.

[95] J. Kuchinka, C. Willems, D. V Telyshev, T. Groth, Control of blood coagulation by hemocompatible material surfaces—a review, Bioengineering 8 (2021) 215, https://doi.org/10.3390/bioengineering8120215.

[96] Y. Yan, L.-C. Xu, E.A. Vogler, C.A. Siedlecki, 1 - contact activation by the intrinsic pathway of blood plasma coagulation, in: C.A.B.T. Siedlecki (Ed.), Hemocompatibility Biomater. Clin. Appl., Woodhead Publishing, 2018, pp. 3–28, https://doi.org/10.1016/B978-0-08-100497-5.00001-X.

[97] A. Sakamoto, H. Jinnouchi, S. Torii, R. Virmani, A. V Finn, Understanding the impact of stent and scaffold material and strut design on coronary artery thrombosis from the basic and clinical points of view, Bioengineering 5 (2018) 71, https://doi.org/10.3390/bioengineering5030071.

[98] S.H. Im, D.H. Im, S.J. Park, Y. Jung, D.-H. Kim, S.H. Kim, Current status and future direction of metallic and polymeric materials for advanced vascular stents, Prog. Mater. Sci. 126 (2022) 100922, https://doi.org/10.1016/j.pmatsci.2022.100922.

[99] J. Gonzalez, R.Q. Hou, E.P.S. Nidadavolu, R. Willumeit-Römer, F. Feyerabend, Magnesium degradation under physiological conditions – best practice, Bioact. Mater. 3 (2018) 174–185, https://doi.org/10.1016/j.bioactmat.2018.01.003.

[100] Z.-Q. Zhang, Y.-X. Yang, J.-A. Li, R.-C. Zeng, S.-K. Guan, Advances in coatings on magnesium alloys for cardiovascular stents – a review, Bioact. Mater. 6 (2021) 4729–4757, https://doi.org/10.1016/j.bioactmat.2021.04.044.

[101] C. Pan, Y. Zhao, Y. Yang, M. Yang, Q. Hong, Z. Yang, Q. Zhang, Immobilization of bioactive complex on the surface of magnesium alloy stent material to simultaneously improve anticorrosion, hemocompatibility and antibacterial activities, Colloids Surf. B Biointerfaces 199 (2021) 111541, https://doi.org/10.1016/j.colsurfb.2020.111541.

[102] Z. Zhen, X. Liu, T. Huang, T. Xi, Y. Zheng, Hemolysis and cytotoxicity mechanisms of biodegradable magnesium and its alloys, Mater. Sci. Eng. C 46 (2015) 202–206, https://doi.org/10.1016/j.msec.2014.08.038.

[103] P.K. Bowen, E.R. Shearier, S. Zhao, R.J. Guillory II, F. Zhao, J. Goldman, J. W. Drelich, Biodegradable metals for cardiovascular stents: from clinical concerns to recent Zn-alloys, Adv. Healthcare Mater. 5 (2016) 1121–1140, https://doi.org/10.1002/adhm.201501019.

[104] R. Yue, J. Niu, Y. Li, G. Ke, H. Huang, J. Pei, W. Ding, G. Yuan, In vitro cytocompatibility, hemocompatibility and antibacterial properties of biodegradable Zn-Cu-Fe alloys for cardiovascular stents applications, Mater. Sci. Eng. C 113 (2020) 111007, https://doi.org/10.1016/j.msec.2020.111007.

[105] Y. Tamura, The role of zinc homeostasis in the prevention of diabetes mellitus and cardiovascular diseases, J. Atherosclerosis Thromb. 28 (2021) 1109–1122, https://doi.org/10.5551/jat.RV17057.

[106] V. Ollivier, C. Roques, N. Receveur, M. Gratz, L. Feldman, D. Letourneur, C. Gachet, P.H. Mangin, M. Jandrot-Perrus, Bioreactivity of stent material: activation of platelets, coagulation, leukocytes and endothelial cell dysfunction in vitro, Platelets 28 (2017) 529–539, https://doi.org/10.1080/09537104.2016.1252836.

[107] D.E.J. Anderson, H.H. Le, H. Vu, J. Johnson, J.E. Aslan, J. Goldman, M.T. Hinds, Thrombogenicity of biodegradable metals, Bioact. Mater. 38 (2024) 411–421, https://doi.org/10.1016/j.bioactmat.2024.05.002.

[108] H. Wu, L. Yang, R. Luo, L. Li, T. Zheng, K. Huang, Y. Qin, X. Yang, X. Zhang, Y. Wang, A drug-free cardiovascular stent functionalized with tailored collagen supports in-situ healing of vascular tissues, Nat. Commun. 15 (2024) 735, https://doi.org/10.1038/s41467-024-44902-2.

[109] C. Chalony, L. Erik Aguilar, C. Hee Park, C. Sang Kim, Drug free anti-cell proliferative and anti-platelet adhesion coating for vascular stents via polymeric electrospun fibers, Mater. Lett. 291 (2021) 129545, https://doi.org/10.1016/j.matlet.2021.129545.

[110] Y. Wen, Y. Li, R. Yang, Y. Chen, Y. Shen, Y. Liu, X. Liu, B. Zhang, H. Li, Biofunctional coatings and drug-coated stents for restenosis therapy, Mater. Today Bio. 29 (2024) 101259, https://doi.org/10.1016/j.mtbio.2024.101259.

[111] J. Vishnu, G. Manivasagam, D. Mantovani, A. Udduttula, M.J. Coathup, K. C. Popat, P.-G. Ren, K.G. Prashanth, Balloon expandable coronary stent materials: a systematic review focused on clinical success, Vitr. Mod. 1 (2022) 151–175, https://doi.org/10.1007/s44164-022-00009-w.

[112] S. Kamalian, M.H. Lev, R. Gupta, Chapter 1 - computed tomography imaging and angiography – principles, in: J.C. Masdeu, R.G.B.T. H, C.N. González (Eds.), Neuroimaging Part I, Elsevier, 2016, pp. 3–20, https://doi.org/10.1016/B978-0-444-53485-9.00001-5.

[113] E.S. Pretorius, Chapter 2 - introduction to ultrasound, CT, and MRI, in: E. S. Pretorius, J.A.B.T. R.S.P, E. Solomon (Eds.), Radiol. Secrests Plus, Mosby, Philadelphia, 2011, pp. 13–18, https://doi.org/10.1016/B978-0-323-06794-2.00002-X.

[114] M.H. Lev, R.G. Gonzalez, 17 - CT angiography and CT perfusion imaging, in: A. W. Toga, J.C.B.T. B.M.T.M, E. Mazziotta (Eds.), Brain Mapp. Methods, Academic Press, San Diego, 2002, pp. 427–484, https://doi.org/10.1016/B978-012693019-1/50019-8.

[115] T. Yamazaki, J. Suzuki, R. Shimamoto, T. Tsuji, Y. Ohmoto-Sekine, T. Morita, H. Yamashita, J. Honye, R. Nagai, S. Komatsu, M. Akahane, K. Ohtomo, Diagnostic efficacy for coronary in-stent patency with parameters defined on Hounsfield CT value-spatial profile curves, Radiography 14 (2008) 98–104, https://doi.org/10.1016/j.radi.2006.12.004.

[116] S. Brown, D.L. Bailey, K. Willowson, C. Baldock, Investigation of the relationship between linear attenuation coefficients and CT Hounsfield units using radionuclides for SPECT, Appl. Radiat. Isot. 66 (2008) 1206–1212, https://doi.org/10.1016/j.apradiso.2008.01.002.

[117] S. Ravanbakhsh, C. Paternoster, G. Barucca, P. Mengucci, S. Gambaro, T. Lescot, P. Chevallier, M.-A. Fortin, D. Mantovani, Improving the radiopacity of Fe–Mn biodegradable metals by magnetron-sputtered W–Fe–Mn–C coatings: application for thinner stents, Bioact. Mater. 12 (2022) 64–70, https://doi.org/10.1016/j.bioactmat.2021.10.022.

[118] Q. Wang, X. Yu, X. Chen, J. Gao, D. Shi, Y. Shen, J. Tang, J. He, A. Li, L. Yu, J. Ding, A facile composite strategy to prepare a biodegradable polymer based radiopaque raw material for "Visualizable" biomedical implants, ACS Appl. Mater. Interfaces 14 (2022) 24197–24212, https://doi.org/10.1021/acsami.2c05184.

[119] A.A. Brouziotis, A. Giarra, G. Libralato, G. Pagano, M. Guida, M. Trifuoggi, Toxicity of rare earth elements: an overview on human health impact, Front. Environ. Sci. 10 (2022) 1–14, https://doi.org/10.3389/fenvs.2022.948041.

[120] J.S. Stinson, C.O. Clerc, Radiopaque markers and methods of using the same, USOO6340367B1, https://patents.google.com/patent/US6340367B1/en, 2002.

[121] J.S. Stinson, Bioabsorbable marker having radiopaque constituents, US6174330B1. https://patents.google.com/patent/US6174330B1/en, 2001.

[122] A. Khalilimeybodi, A. Alishzadeh Khoei, B. Sharif-Kashani, Future balloon-expandable stents: high or low-strength materials? Cardiovasc. Eng. Technol. 11 (2020) 188–204, https://doi.org/10.1007/s13239-019-00450-1.

[123] É.Ó. Máirtín, J. Concannon, G. Parry, J.P. McGarry, A mechanistic analysis of delamination of elastic coatings from the surface of plastically deformed stents, Int. J. Solids Struct. 224 (2021) 111051, https://doi.org/10.1016/j.ijsolstr.2021.111051.

[124] S. Tammareddi, Q. Li, Effects of material on the deployment of coronary stents, Adv. Mater. Res. 123–125 (2010) 315–318. https://doi.org/10.4028/www.scientific.net/AMR.123-125.315.

[125] J.S. Soares, J.E. Moore, Biomechanical challenges to polymeric biodegradable stents, Ann. Biomed. Eng. 44 (2016) 560–579, https://doi.org/10.1007/s10439-015-1477-2.

[126] A. Muliana, K.R. Rajagopal, On the response of viscoelastic biodegradable polymeric solids, Mech. Res. Commun. 39 (2012) 51–58, https://doi.org/10.1016/j.mechrescom.2011.10.004.

[127] R.G. Pauck, B.D. Reddy, Computational analysis of the radial mechanical performance of PLLA coronary artery stents, Med. Eng. Phys. 37 (2015) 7–12, https://doi.org/10.1016/j.medengphy.2014.09.014.

[128] A. Schiavone, T.-Y. Qiu, L.-G. Zhao, Crimping and deployment of metallic and polymeric stents – finite element modelling, Vessel Plus 1 (2017) 12–21, https://doi.org/10.20517/2574-1209.2016.03.

[129] M. Shahverdi, S. Seifi, A. Akbari, K. Mohammadi, A. Shamloo, M.R. Movahhedy, Melt electrowriting of PLA, PCL, and composite PLA/PCL scaffolds for tissue engineering application, Sci. Rep. 12 (2022) 19935, https://doi.org/10.1038/s41598-022-24275-6.

[130] O. Glushko, M.J. Cordill, Electrical resistance of metal films on polymer substrates under tension, Exp. Tech. 40 (2016) 303–310, https://doi.org/10.1007/s40799-016-0040-x.

[131] K. Kim, J. Lee, Determination of Nonconductive coating thickness using electrical contact conductance and surface profile, Coatings 8 (2018) 310, https://doi.org/10.3390/coatings8090310.

[132] S. Altaf Husain, P. Kreiml, C.O.W. Trost, D. Faurie, M.J. Cordill, P.-O. Renault, Residual stress and thickness effects on fracture behavior of trilayer films during uniaxial loading, Thin Solid Films 788 (2024) 140173, https://doi.org/10.1016/j.tsf.2023.140173.

[133] R.X. Wang, X.M. Tao, Y. Wang, G.F. Wang, S.M. Shang, Microstructures and electrical conductance of silver nanocrystalline thin films on flexible polymer substrates, Surf. Coating. Technol. 204 (2010) 1206–1210, https://doi.org/10.1016/j.surfcoat.2009.10.030.

[134] T.Y. Qiu, L.G. Zhao, M. Song, A computational study of mechanical performance of bioresorbable polymeric stents with design variations, Cardiovasc. Eng. Technol. 10 (2019) 46–60, https://doi.org/10.1007/s13239-018-00397-9.

[135] S. Khalaj Amnieh, M. Mashayekhi, E. Shahnooshi, M. Tavafoghi, P. Mosaddegh, Biodegradable performance of PLA stents affected by geometrical parameters: the risk of fracture and fragment separation, J. Biomech. 122 (2021) 110489, https://doi.org/10.1016/j.jbiomech.2021.110489.

[136] L. Klinker, S. Lee, J. Work, J. Wright, Y. Ma, L. Ptaszek, R.C. Webb, C. Liu, N. Sheth, M. Mansour, J.A. Rogers, Y. Huang, H. Chen, R. Ghaffari, Balloon catheters with integrated stretchable electronics for electrical stimulation, ablation and blood flow monitoring, Extrem. Mech. Lett. 3 (2015) 45–54, https://doi.org/10.1016/j.eml.2015.02.005.

[137] E.H. Gunday, L.J. Gerrans, L. Chu, Electrically conductive balloon catheter, WO2012154358A1. https://patents.google.com/patent/WO2012154358A1/en, 2012.

[138] J. Zhao, G. Song, Q. Zhao, H. Feng, Y. Wang, J.M. Anderson, H. Zhao, Q. Liu, Development of three-dimensionally printed vascular stents of bioresorbable poly (l-lactide-co-caprolactone), J. Biomed. Mater. Res. Part B Appl. Biomater. 111 (2023) 656–664, https://doi.org/10.1002/jbm.b.35184.

[139] A. Thakur, U.K. Vates, S. Mishra, Proof of concept study for radial compression strength & shape memory effect of 3D printed double arrowhead PLA stent, Emerg. Mater. (2024), https://doi.org/10.1007/s42247-024-00751-9.

[140] X. Han, X. Wu, M. Kelly, X. Chen, Fabrication and optimal design of biodegradable polymeric stents for aneurysms treatments, J. Funct. Biomater. 8 (2017) 8, https://doi.org/10.3390/jfb8010008.

[141] World Health Organization (WHO), Hypertension (2024). https://www.who.int/news-room/fact-sheets/detail/hypertension. (Accessed 6 August 2024).

[142] A. V Poznyak, N.K. Sadykhov, A.G. Kartuesov, E.E. Borisov, A.A. Melnichenko, A. V Grechko, A.N. Orekhov, Hypertension as a risk factor for atherosclerosis: cardiovascular risk assessment, Front. Cardiovasc. Med. 9 (2022), https://doi.org/10.3389/fcvm.2022.959285.

[143] J.-P. Barral, A. Croibier, 2 - circulatory physiology, in: J.-P. Barral, A.B.T. Croibier (Eds.), Visc. Vasc. Manip., Churchill Livingstone, Oxford, 2011, pp. 27–45, https://doi.org/10.1016/B978-0-7020-4351-2.00002-8.

[144] H. Bakhtiari, A. Nouri, M. Tolouei-Rad, Impact of 3D printing parameters on static and fatigue properties of polylactic acid (PLA) bone scaffolds, Int. J. Fatig. 186 (2024) 108420, https://doi.org/10.1016/j.ijfatigue.2024.108420.

[145] X. Chen, Y. Huang, C. Chen, J. Lu, X. Fan, Experimental study and analytical modeling on hysteresis behavior of plain concrete in uniaxial cyclic tension, Int. J. Fatig. 96 (2017) 261–269, https://doi.org/10.1016/j.ijfatigue.2016.12.002.

[146] M. Mansour, K. Tsongas, D. Tzetzis, Measurement of the mechanical and dynamic properties of 3D printed polylactic acid reinforced with graphene, Polym. Technol. Mater. 58 (2019) 1234–1244, https://doi.org/10.1080/03602559.2018.1542730.

[147] J.A. Panadero, L. Vikingsson, J.L. Gomez Ribelles, S. Lanceros-Mendez, V. Sencadas, In vitro mechanical fatigue behavior of poly-ε-caprolactone macroporous scaffolds for cartilage tissue engineering: influence of pore filling by a poly(vinyl alcohol) gel, J. Biomed. Mater. Res. Part B Appl. Biomater. 103 (2015) 1037–1043, https://doi.org/10.1002/jbm.b.33276.

[148] Z. Meng, J. He, Z. Cai, F. Wang, J. Zhang, L. Wang, R. Ling, D. Li, Design and additive manufacturing of flexible polycaprolactone scaffolds with highly-tunable mechanical properties for soft tissue engineering, Mater. Des. 189 (2020) 108508, https://doi.org/10.1016/j.matdes.2020.108508.

[149] X. Liang, J. Gao, W. Xu, X. Wang, Y. Shen, J. Tang, S. Cui, X. Yang, Q. Liu, L. Yu, J. Ding, Structural mechanics of 3D-printed poly(lactic acid) scaffolds with tetragonal, hexagonal and wheel-like designs, Biofabrication 11 (2019) 35009, https://doi.org/10.1088/1758-5090/ab0f59.

[150] J. Zhang, V. Hirschberg, D. Rodrigue, Mechanical fatigue of biodegradable polymers: a study on polylactic acid (PLA), polybutylene succinate (PBS) and polybutylene adipate terephthalate (PBAT), Int. J. Fatig. 159 (2022) 106798, https://doi.org/10.1016/j.ijfatigue.2022.106798.

[151] N. Filipovic, D. Nikolic, I. Isailovic, M. Milosevic, V. Geroski, G. Karanasiou, M. Fawdry, A. Flanagan, D. Fotiadis, M. Kojic, In vitro and in silico testing of partially and fully bioresorbable vascular scaffold, J. Biomech. 115 (2021) 110158, https://doi.org/10.1016/j.jbiomech.2020.110158.

[152] 2 - the basic properties of building materials, in: H.B.T. B.M, C.E. Zhang (Eds.), Woodhead Publ. Ser. Civ. Struct. Eng., Woodhead Publishing, 2011, pp. 7–423, https://doi.org/10.1533/9781845699567.7.